Spring 2016

Experimental and Numerical Investigation of Aerodynamic Performance for Vertical-Axis Wind Turbine Models with Various Blade Designs

Travis E. Salyers

EXPERIMENTAL AND NUMERICAL INVESTIGATION OF AERODYNAMIC

PERFORMANCE FOR VERTICAL-AXIS WIND TURBINE MODELS

WITH VARIOUS BLADE DESIGNS

by

TRAVIS EVANDA SALYERS

(Under the Direction of Mosfequr Rahman)

ABSTRACT

The demand for wind energy as a renewable source is rising substantially. A growing interest exists in utilizing potential energy conversion applications in areas with less powerful and less consistent wind conditions. In these areas, vertical-axis wind turbines (VAWTs) possess several advantages over the conventional horizontal-axis type. Savonius turbines are drag-based rotors which operate due to a pressure difference between the advancing and retreating blades. These turbines are simpler in design, less expensive to install, non-dependent of wind direction, and more efficient in lower wind speeds. In the present study, six different rotor designs with equal swept areas are analyzed with wind tunnel testing and numerical simulations. These models include a traditional Savonius with 2 blades, "CC" model, "QM" model, and 90 degree helical twist models with 2, 3, and 4 blades. The models were designed using the CAD software SolidWorks. Due to the complex geometry of the blades, the physical models were then 3D printed for experimental testing. Subsonic, open-type wind tunnel testing was used for measuring RPM and reactional torque over a range of wind speeds. For the numerical approach, ANSYS Fluent simulations were used for analyzing aerodynamic performance by utilizing moving reference frame and sliding mesh model techniques. For the models with helical twist, the cross-sections of the blades varies in the Y-direction. Because of this, a 3-dimensional and transient

method was used for accurately solving torque and power coefficients. The 5 new rotor geometries included in the study create a center of pressure further from the axis of rotation causing greater torque on the turbine shaft, compared to the traditional Savonius turbine. The CC and QM cross-sections reduce the total range of negative torque on the blades by 20 degrees, compared to the traditional Savonius model. Helical designs better spread the applied torque over a complete revolution resulting in positive torque over all operational angles. Helical models with 2 and 3 blades have the best self-starting capability in low wind speeds. Under no generator loading, Helical3 begins rotation of 35 RPM at just 1.4 m/s wind velocity. The highest power coefficient in the study is achieved, both experimentally and numerically, by the helical VAWT with 2 blades. Averaged over one full rotation, a maximum power coefficient of 0.14 is observed with the Helical2 model at tip-speed ratio of 0.475.

INDEX WORDS: Vertical-axis wind turbine, VAWT, Savonius, Helical, Wind tunnel, Computational fluid dynamics, CFD, ANSYS Fluent

EXPERIMENTAL AND NUMERICAL INVESTIGATION OF AERODYNAMIC

PERFORMANCE FOR VERTICAL-AXIS WIND TURBINE MODELS

WITH VARIOUS BLADE DESIGNS

by

TRAVIS EVANDA SALYERS

B.S., Georgia Southern University, 2014

A Thesis Submitted to the Graduate Faculty of Georgia Southern University in

Partial Fulfillment of the Requirements for the Degree

MASTER OF SCIENCE

STATESBORO, GEORGIA

EXPERIMENTAL AND NUMERICAL INVESTIGATION OF AERODYNAMIC

PERFORMANCE FOR VERTICAL-AXIS WIND TURBINE MODELS

WITH VARIOUS BLADE DESIGNS

by

TRAVIS EVANDA SALYERS

Major Professor: Mosfequr Rahman

Committee: Minchul Shin

Valentin Soloiu

Electronic Version Approved:

May 2016

DEDICATION

This work is dedicated to my parents for their endless support in all of my endeavors.

ACKNOWLEDGEMENTS

I would like to acknowledge Dr. Mosfequr Rahman for his guidance and direction throughout my research in his wind energy laboratory. I want to thank Dr. Minchul Shin and Dr. Valentin Soloiu for taking time to be a part of my thesis committee and reviewing this work. I also want to thank Donald Tankersley and Emile Maroha for their assistance with the wind tunnel fabrication.

TABLE OF CONTENTS

LIST OF SYMBOLS

A	Swept Area (m^2)
CFD	Computational Fluid Dynamics
C_m	Moment Coefficient
C_p	Power Coefficient
D	Blade Diameter (m)
H	Blade Height (m)
N	Rotations per Minute
TSR	Tip-Speed Ratio
T	Torque ($N\text{-}m$)
V	Wind Velocity (m/s)
VAWT	Vertical-Axis Wind Turbine
ρ	Air Density (kg/m^3)
ω	Angular Velocity (rad/s)
λ	Tip-Speed Ratio

LIST OF TABLES

LIST OF FIGURES

CHAPTER 1

INTRODUCTION

1.1 Problem statement

The need for improved alternative energy sources is ever prevalent. Wind energy is one of the most viable renewable sources today due to its year-round availability, and pollution-free nature. According to the *Wind Vision Report*, published by the U.S. Department of Energy, wind energy is the largest source of added renewable energy generation in the United States since 2000. A plan has been set by the program for 20% of the nation's electricity to be supplied by wind by the year 2030, and 35% by 2050. The report states that a key to achieving this goal is to improve the potential of low-wind-speed locales ("ENERGY.GOV," 2016). Because of this, many works are underway involving the efficiency of wind energy conversion systems, especially for regions with low average wind velocities.

The two primary types of conversion systems are the horizontal-axis wind turbine (HAWT) and the vertical-axis wind turbine (VAWT). HAWTs have been in practice for some time and are heavily favored over VAWTs for large-scale power generation; however, research of VAWTs has gained growing interest in recent years because of the opportunities available for small-scale and off-grid power generation which favors the use of vertical-axis turbines. The design and testing of 3D printed vertical-axis wind turbine models is presented in this work.

1.2 VAWT advantages

Vertical-axis wind turbines have many advantages for small scale wind energy applications. Interest in VAWT technology has recently grown due to potential for off-grid power supply in several different applications. One of the greatest advantages for VAWTs over traditional HAWTs is the ability to self-start in some designs. Under low wind speed conditions,

many VAWTs begin to rotate without the added expense of actuators or controls. For VAWTs the generator may be located on the ground rather than high in the air. This provides much more convenient and cost efficient installation and maintenance than that of HAWTs. Another advantageous feature of VAWTs is the fact that they can accept wind from all directions. Regardless of where the wind is coming from, the turbines generally perform equally as well. For this reason, VAWTs are preferred over HAWTs where unsteady and low speed wind conditions exist.

1.3 Savonius type

Drag-based VAWT designs are referred to as Savonius type. The first Savonius turbine was developed in 1922 and was made up of semi-circle blades (MacPhee, David, and Beyene 2012). Conventional Savonius rotors with two and three blades are displayed in Figure 1.1.
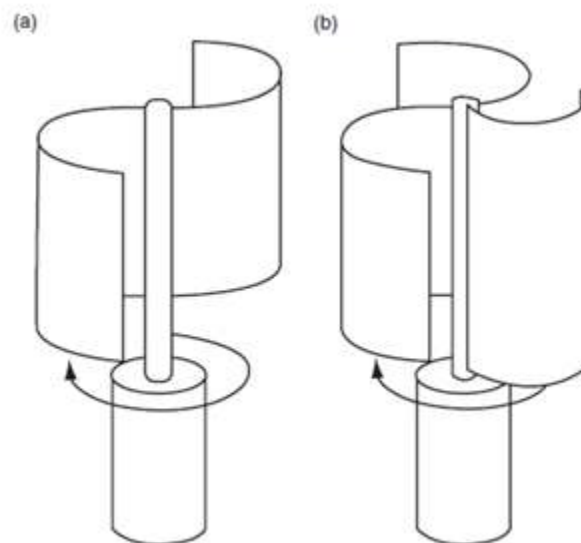
Figure 1.1. Savonius rotors with (a) two blades and (b) three blades (MacPhee, David, and Beyenne, 2012)

This type of turbines rotates due to a difference in drag caused by the shape and orientation of the blades. The blade moving with the wind experiences more drag than the blade moving against the wind due to the curvatures.

1.4 Darrieus type

The other type of VAWT is lift-based turbines, known as Darrieus type. The most commonly used Darrieus turbines include the Egg-Beater, H-type, and Gyromill designs. These common designs can be seen in Figure 1.2.
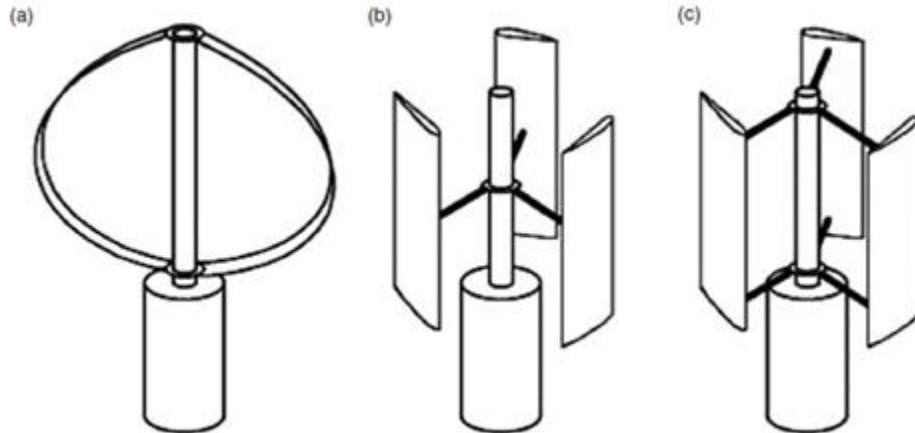
Figure 1.2. Darrieus type rotor designs: Egg-beater (a), H-type (b), and Gyromill (c) (MacPhee, David, and Beyenne, 2012)

Darrieus rotors produce higher power coefficient, or efficiency, at higher wind speeds, but do not enjoy the same self-starting ability of Savonius turbines at lower wind speeds. When experiencing high rotational speeds, though, Darrieus type VAWTs typically produce more power than drag-based designs (MacPhee, David, and Beyene 2012).

1.5 Scope of research

In the present study, six different rotor designs are analyzed with wind tunnel testing and numerical simulations. These models include a traditional Savonius with 2 blades, "CC" model, "QM" model, and 90 degree helical twist models with 2, 3, and 4 blades. Wind tunnel experiments are conducted to find reactional torque and rotations per minute (RPM) from which turbine efficiencies are calculated. Computational Fluid Dynamic (CFD) simulations are

performed with ANSYS Fluent to study aerodynamic characteristics of the models. The objectives of the research are as follows:

- Increase power coefficient of Savonius turbines by creating new blade geometries

- Determine the self-starting capabilities of the new models

- Design and implement new test fixtures to accompany 3D printed turbines

- Develop a three-dimensional and transient model for VAWT simulation

- Improve the existing subsonic wind tunnel by fabricating a new model test section

It is hypothesized that the new "CC" and "QM" models will achieve higher maximum torque and power coefficients than the conventional Savonius model. Also, the helical models will create positive torque on the turbine shaft over all operational angles of rotation and possess the ability to self-start in lower wind speeds, increasing overall performance.

1.6 Contributions to scientific knowledge

This research provides several contributions to the vertical-axis wind turbine body of knowledge. First, few have developed a three-dimensional dynamic analysis using ANSYS Fluent commercial software for the study of VAWTs. A detailed approach of the 3D, transient simulation is outlined in this thesis. New blade geometries are tested and compared to standard Savonius rotors. These models are produced with new 3D printing technology. Recommendations for future work are provided to further improve VAWT performance based on the findings of this research.

1.7 Organization of the thesis

The work completed in this thesis is presented as follows. A comprehensive literature review of current VAWT technologies is organized in Chapter 2. The review covers drag-based

wind turbine technologies. Several papers are reviewed relating to the performance of Savonius turbine geometry. Methods for experimentation and numerical analysis are discussed.

The experimental and numerical methodology for completing the research is described in Chapter 3. Design of test setups and equipment for wind tunnel experiments is included as well as methodology for the ANSYS Fluent simulations. Additionally, mathematical expressions are provided for calculating wind turbine efficiency.

The results and analysis for each model tested is covered in Chapter 4. The results are primarily broken down into two sections: experimental and numerical. The findings of the study are discussed in terms of self-starting ability, aerodynamic performance, and power coefficient.

A summary of the results from this research along with recommendations for future work are presented in Chapter 5. Additional information related to the work, including experimental and numerical data, is available in the appendices.

CHAPTER 2

LITERATURE REVIEW

2.1 Overview

Many researchers are working to enhance performance of vertical axis wind turbines both numerically and experimentally. These works vary from computational simulations to laboratory measurements on actual models. There are two primary goals when considering VAWT research. The first is improving conversion efficiency of Savonius rotors by reducing drag losses. The second is improving self-starting characteristics of Darrieus type rotors in order to increase overall conversion efficiency for realistic wind conditions.

There are three important non-dimensional coefficients that characterize turbine performance. Tip-speed ratio (*TSR*) is the ratio of blade tip speed to the free-stream wind velocity. It is the product of angular velocity and overall radius, divided by the wind velocity. A schematic for tip-speed ratio is provided in Figure 2.1.
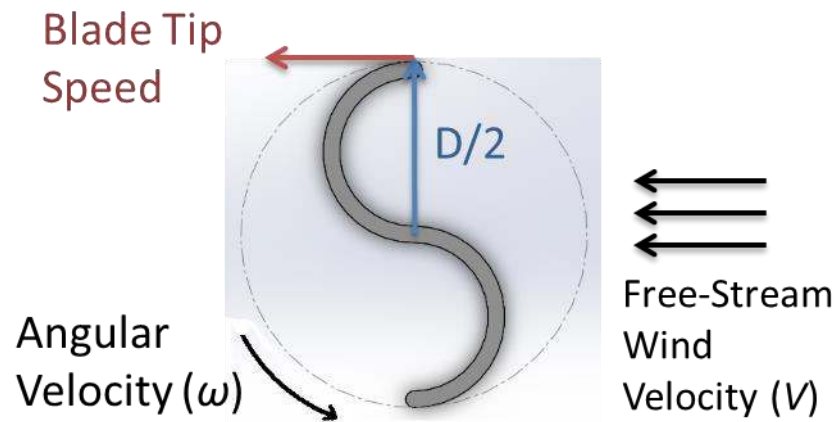
Figure 2.1. Tip-speed ratio schematic

The moment coefficient (*Cm*), also known as the torque coefficient, characterizes the amount of torque generated by the blade geometry. It is the measured torque divided by the theoretical torque value available in the wind. Power coefficient is the product of tip-speed ratio and

moment coefficient. The power coefficient is the efficiency of the turbine. Procedures for calculating each of these non-dimensional coefficients is available in the analysis section of Chapter 3 in the thesis. A useful way for comparing the efficiencies of different wind turbine designs is plotting the power coefficient vs. tip-speed ratio. A graph comparing various types of wind conversion systems can be seen in Figure 2.2 (Morshed, Rahman, and Ahmed, 2013).
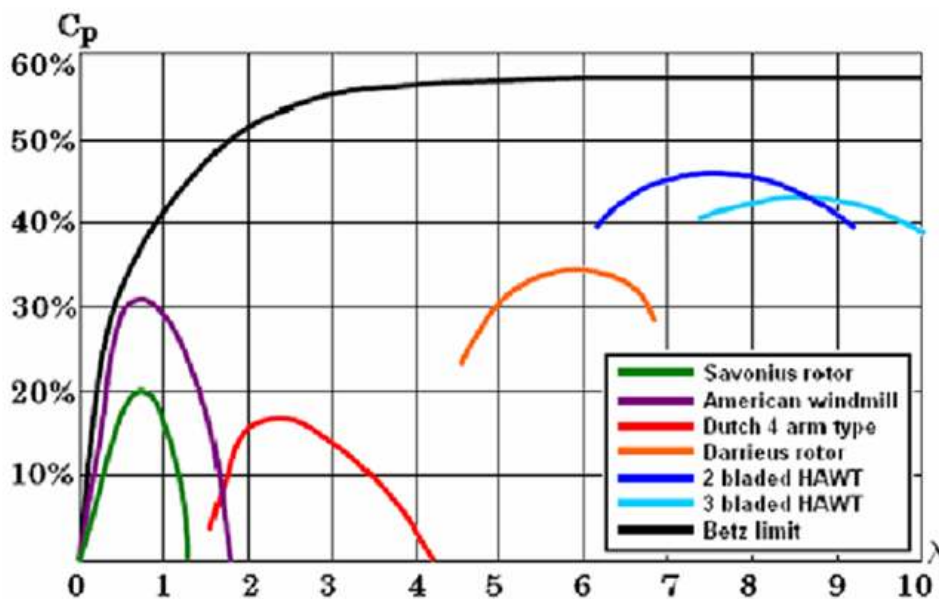
Figure 2.2. Power coefficient vs. tip-speed ratio for various wind turbine types (Morshed, Rahman, and Ahmed, 2013)

Savonius VAWTs operate in a tip-speed ratio range of 0 to 1.2 and have a maximum efficiency of 20 percent. Darrieus rotors operate in higher wind speeds and achieve a maximum efficiency of 35 percent, while HAWTs enjoy the highest power coefficients of any turbine type. This chapter provides a discussion of the various works involving performance improvement of VAWTs for low-wind-speed locales.

2.2 Savonius research

Savonius wind turbines are drag-type VAWTs with negligible lift forces. The traditional Savonius rotor is made up of two opposite-facing semicircular buckets. Rotation is caused due to

a difference in pressure between the advancing and retreating blades. When wind strikes the blades of the turbine, two components of drag force are generated on each blade surface. Normal drag force (Fn) acts perpendicular to the blade wall and tangential drag force (Ft) acts along the tangential direction of each blade (Bashar, Rahman, and Khan, 2013). The schematic diagram of the Savonius rotor cross-section with the components of drag forces on each blade is shown in Figure 2.3.
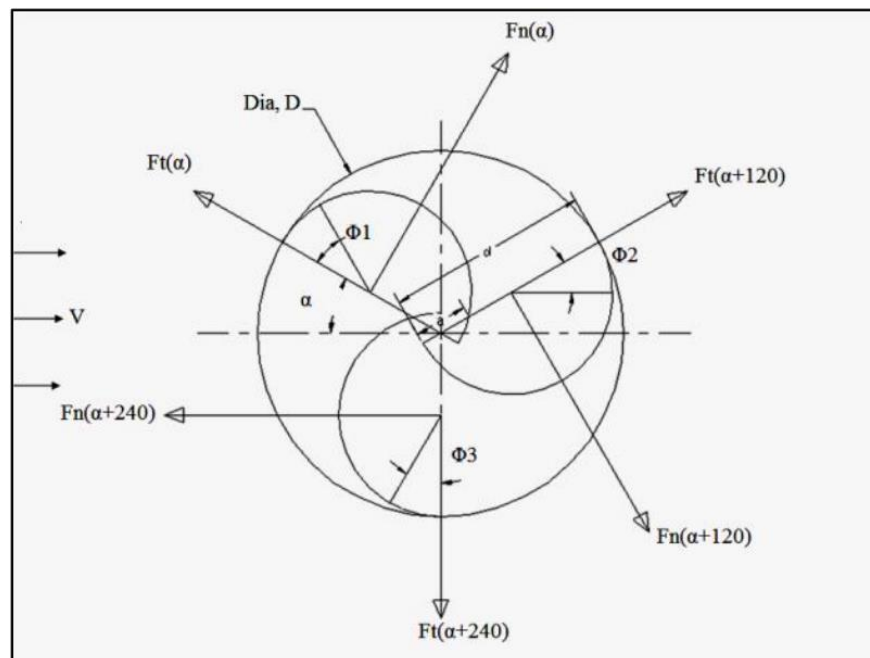
Figure 2.3. Schematic of the drag force components on model cross-section (Bashar, Rahman, and Khan 2013)

Drag-based Savonius VAWTs exemplify high starting torque and perform best at low tip-speed ratios. Much research has been conducted regarding two and three blade rotors of this type. Morshed, Rahman, and Ahmed (2013) provided analysis of three-bladed Savonius rotors with different overlap ratios. Models with overlap ratio of 0.12 and 0.26 were compared to a model with no overlap. A numerical investigation using GAMBIT and FLUENT was conducted along with wind tunnel experimentation. The overlap ratio of 0.12 can be seen from the top view drawing in Figure 2.4.
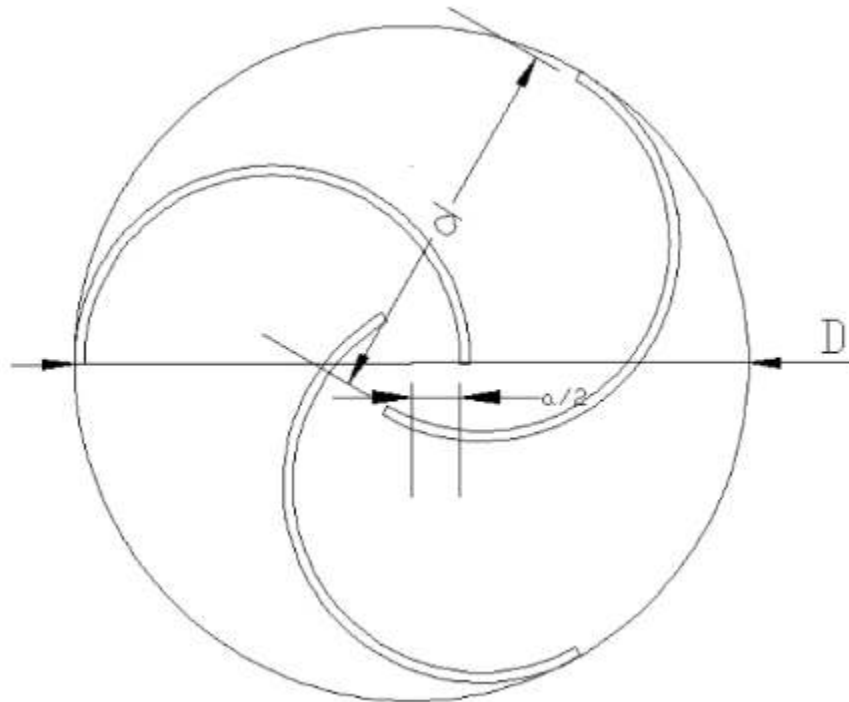
Figure 2.4. Top view of Savonius model with overlap ratio of 0.12 (Morshed, Rahman, and Ahmed, 2013)

It was concluded in the study that for all tested wind speeds, the model with 0.12 overlap attained the highest experimental torque coefficient. At higher wind speeds the same model demonstrated the best experimental power coefficient; however, the model with no overlap had the better power coefficient at low wind speed.

Rather than conventional Savonius types, some have investigated alternative drag-based designs. Ghatage et al (2012) researched the effects of twisted rotors. It was found that twisting the blades provided enhanced efficiency of the turbine. The experimental results agreed with CFD simulations. It was also concluded that a twisted two-blade arrangement outperformed a twisted design with three blades. The optimum twist angle for this study was found to be 30°. The use of stacked Savonius rotors also show increases in wind conversion efficiency compared to a single rotor (Abraham et al 2011). This is one promising example of a multistage turbine. Several other improvements to conventional drag-type rotors were also implemented in this case.

Circular caps were added to the top and bottom of the blades. Venting apertures were applied to the middle of the rotating blades in an attempt to reduce advancing drag. The vents are pictured in Figure 2.5.
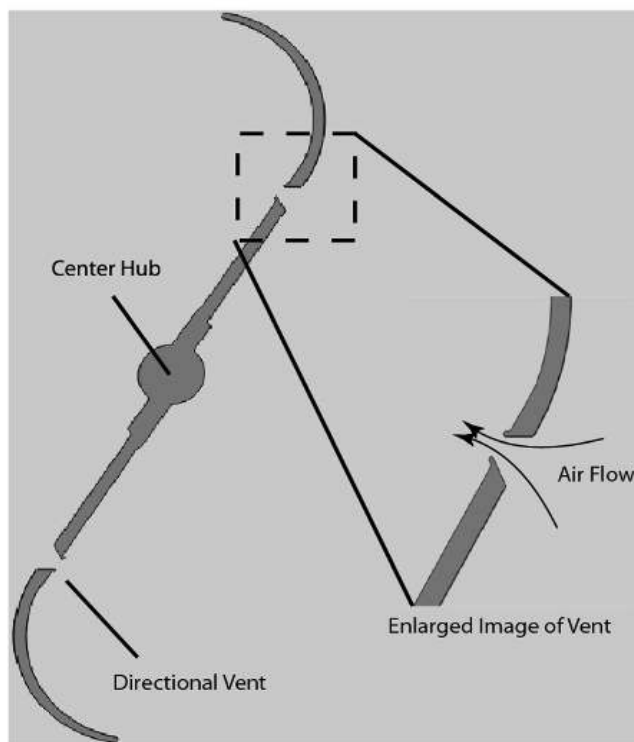
Figure 2.5. Directional vents for reducing drag on advancing blade (Abraham et al. 2011)

The proposed vertical axis turbine by Abraham et al (2011) met specific needs for powering an off-grid cellular tower. The research concluded that the added caps and vents increased performance of rotors by increasing drag on the retreating blade side while decreasing drag on the advancing side. Another attempt to reduce advancing drag was completed by Altan and Atilgan (2008) with the use of curtains. The curtains directed flow to the retreating side by blocking flow to the convex blade on the advancing side. The curtain arrangement can be seen in Figure 2.6.
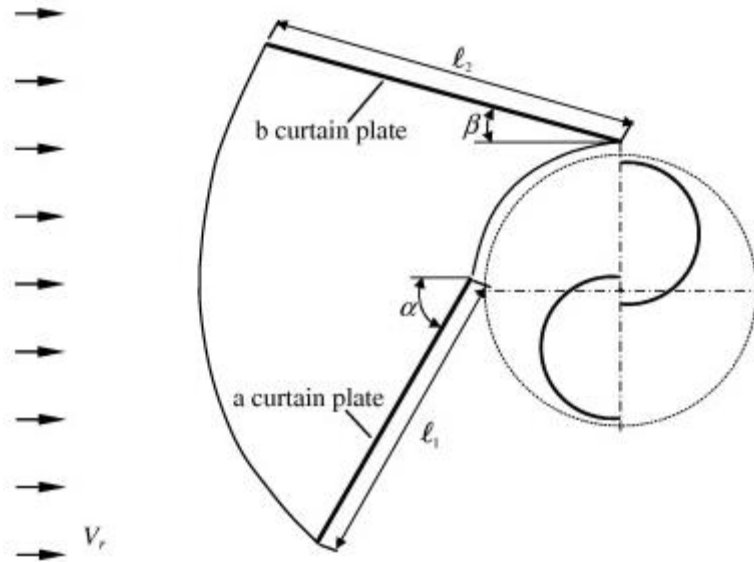
Figure 2.6. Curtain arrangement in front of Savonius rotor (Altan and Atilgan 2008)

Static torque measurements were taken on the blades with and without the curtain. The best results were obtained from use of the curtain. Different curtain lengths were then used, and long curtain dimensions provided significantly higher static torque values. The results of the experiment agreed with numerical analysis which was completed with FLUENT 6.0 trade software.

2.3 Helical twisted blades

The traditional Savonius rotor consists of 2 opposite facing semicircular buckets and constant cross-section. The addition of a helical twist to the blade tips alters turbine performance (Lee et al. 2016). An example Savonius rotor and one with helical twist, developed by Can et al. (2013), may be seen in Figure 2.7.

(a)   (b)
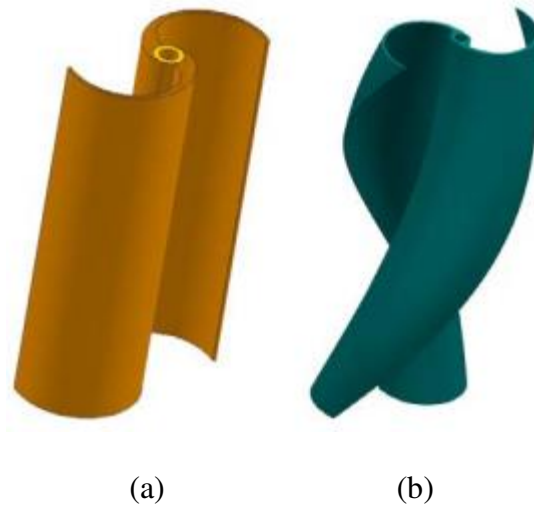
Figure 2.7. Conventional Savonius turbine (a) and turbine with helical twist (b) (Can et al. 2013)

It was found that the Savonius rotor produced a negative torque coefficient within two narrow

ranges of rotation, reflecting an intermittent disturbance to the flow field. In contrast, the torque

coefficient for the spiral design remained positive during the entire rotational cycle. The

maximum torque coefficient (Cq) for the twisted blade was 0.43 while the maximum Cq

recorded with the traditional bade was less than 0.30 with more severe fluctuation (Can et al.

2013). In addition to a standard S-blade (Savonius) and helical rotor, Diaz et al. (2015) added a

three-bladed Savonius model and a two-stage model to their study. The helical rotor showed a

20% improvement in efficiency over the other models, and the three-bladed Savonius model

attributed the lowest recorded power coefficient in the study. In another study, numerical

analysis was performed on a Savonius rotor with 45 degree twist angle. It was found that

significant power coefficient increase occurred at rotor angle of 90 degrees in respect to

incoming air velocity (Bachu, Gupta, and Misra 2013). Saha and Rajkumar (2006) concluded

that varying twist angle on Savonius turbines with three blades affects starting performance. All

twist angles in the study, from 0 to 25 degrees, improved the self-starting characteristics. Larger

twist angles were recommended for lower wind velocities, and the 15 degree twist model

produced maximum power coefficient. Kamoji et al. (2009) proposed a helical Savonius rotor with a 90 degree twist angle. It was found that torque coefficient remained positive for all operating angles, and the maximum power coefficient was obtained by the helical model with no overlap, no shaft, and aspect ratio of 0.88. Ricci et al. (2016) developed different configurations of Savoinus rotors for the purpose of street lighting applications. The experiment was conducted in a closed loop wind tunnel. Three models were tested: straight blade, 90 degree twist, and 105 degree twist. The best results were obtained with the 105 degree twist helical rotor with end plates and central gap. The maximum *Cp* of 0.251 occurred at tip-speed ratio of 0.899.

2.4 Addition of end plates

The effects of various end plates were presented by Jeon et al. (2014). The researchers added four different end plates of various shape and size to helical models. The twist angle for these models 180 degrees. The use of end plates on top and bottom increased the power coefficient by up to 36%, compared to a model with no end plates. It was determined that circular plates with area the same as that of the swept area of the turbine maximized power.

2.5 Blade overlap conditions

Overlapping the blades allows for airflow to occur between them, and the overlap condition is defined by the gap between blade and shaft, relative to the turbine radius. Deb et al. (2014) experimented with a 20 degree twist helical Savonius rotor at different overlap conditions. Six different overlap ratios ranging from 0 to 20% were investigated. It was concluded that rotor performance increases with increasing overlap ratio up to a certain limit. The maximum power coefficient obtained was 0.289 with an overlap ratio of 12.76%. The recommended tip-speed ratio for best performance of this design was 0.51-0.90.

2.6 Changing number of blades

A study performed by Wenehenubun et al. (2015) addressed the influence of increasing number of blades on turbine rotation. Two, three, and four straight-blade Savonius models were analyzed with wind tunnel testing and numerical simulation using ANSYS software. It was found that the four blade turbine performed best at lower tip-speed ratios. At higher tip-speed ratios, the model with three blades produced the highest power coefficient. Saha et al. (2008) found that for multistage systems, maximum power coefficient is produced with two twisted blades and two stages.

2.7 Darrieus research

Lift-based VAWTs is a popular research area because of the higher power coefficient potential. Typically Darrieus rotors consist of straight, vertical airfoils. The most prevalent work in this area is the optimization of airfoil shape. This is done by testing different designs by the use of two-dimensional Computational Fluid Dynamics. Aerodynamic investigations are performed numerically in order to improve maximum output torque and power coefficients (Mohamed 2012).

Designs for lift-based VAWTs are not limited to only vertical blades. Armstrong et al (2012) analyzed the effects of canted blades and canted blades with fences in comparison to straight blades. The turbine with canted blades is shown in Figure 2.8.
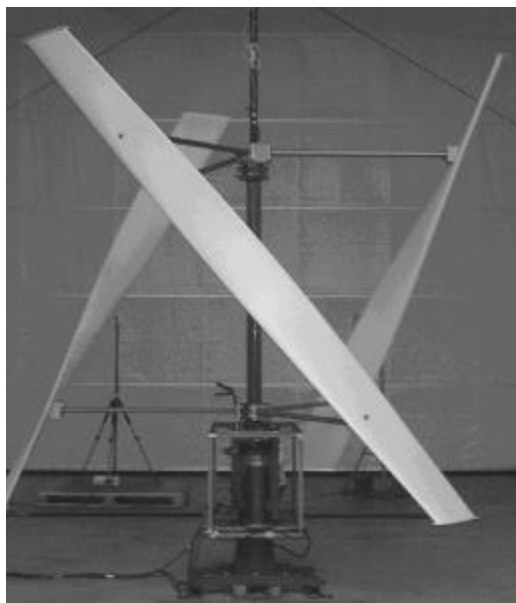
Figure 2.8. Derrieus-type turbine with canted blades (Armstrong et al. 2012)

The straight-blade and canted-blade H-Darrieus turbines were tested at very high Reynolds numbers. The experiment indicated that rotors with canted blades experienced much less flow reversal than that of the vertical blades. The addition of fences on the canted blades increased power and decreased the tip-speed ratio at which maximum power occurred.

2.8 Self-starting performance

Much work is being done in the area of self-starting turbines. The ability for a turbine to start rotation at low wind speeds improves overall performance. Also, the absence of sensors and controllers can greatly reduce cost. Savonius rotors typically enjoy better self-starting performance than Darrieus types. Many techniques have been researched to improve the start-up of lift-based Darrieus rotors. Beri, Habtamu, and Yingxue (2011) performed simulations of modified airfoils with a hinged tail using FLUENT. A conventional NACA0018 airfoil model was allowed to flex 15° at the trailing edge. The hinge was located back 70% of the blade length. Moving mesh technique was utilized to investigate two-dimensional flow around the model. Unsteady flow simulations were performed at low tip-speed ratios ranging from 0.1 to 1.0 and

compared to simulations of a known self-starting airfoil model. The simulation results indicated that the hinged model had better self-starting performance for all flow conditions.

2.9 Multistage turbines

Another effort to enhance performance of VAWTs involves stacking multiple rotors on one axis. Multistage turbines consist of at least two tiers containing separate blade configurations. Gorelev and Krivopitsky (2008) designed two-tier wind turbines made up of straight-bladed Darrieus rotors. The full-scale models achieved self-start rotation without any added devices. Two separate configurations were fabricated with levels of staggered airfoils. The first used six blades in total of three on top and three on bottom. The second model was built with two blades on the top tier and two on the bottom. Of all the experimental tests, a maximum efficiency of 40% was reached for a 3kW apparatus.

2.10 Hybrid research

Hybrid VAWTs include combinations of multiple types of rotors in one turbine. The goal of hybrid turbines is to attain higher power coefficient or better starting performance than in one type of rotor alone. Gavalda, Massons, and Diaz (1990) experimented with a Darrieus and Savonius hybrid turbine. The central part of the turbine was a Savonius drag-based rotor. Outstretched armatures contained lift-based Darrieus blades. Their design was successful in achieving higher starting torque than that of the Darrieus only rotor. An example of this type of hybrid configuration is depicted in Figure 2.9.
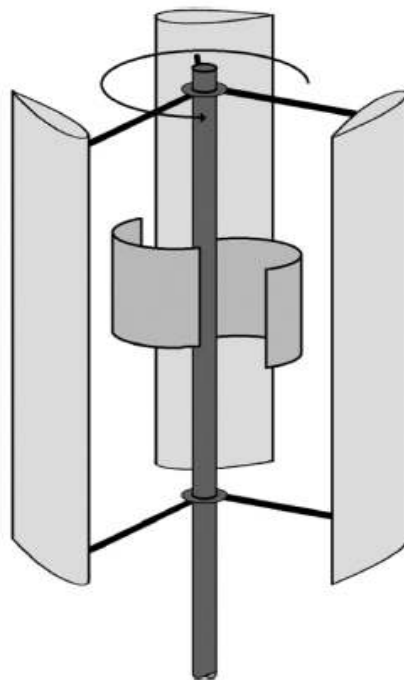
Figure 2.9. Typical hybrid turbine consisting of Savonius and Darrieus rotors (MacPhee, David, and Beyenne, 2012)

Work by Kou et al (2011) involved a multitier Savonius rotor combined with a three-bladed Darrieus gyromill rotor. The addition of the Savonius rotor enhanced conversion efficiency compared to only gyromill. Also, the required wind speed for self-starting was successfully lowered for the hybrid design. Gupta, Biswas, and Sharma (2008) combined a Savonius with an egg-beater type Darrieus rotor. Their design consisted of three-bladed Darrieus and three-bladed Savonius. Varying overlap ratios were implemented in the Savonius rotor. The model was tested in a subsonic wind tunnel and compared to a simple Savonius rotor. For the hybrid turbine configuration, it was found that maximum performance occurred with no overlap geometry in the Savonius rotor. It was concluded in the study that the power coefficient was significantly greater for the hybrid model than for that of the Savonius rotor at all overlap conditions.

Few researchers have explored the performance of hybrid VAWTs consisting of drag-based rotors along with unsymmetrical lift-based airfoil blades. The Darrieus H-type rotor has

among the highest power coefficients of any VAWT design, but it does not exhibit good starting behavior. This is due to the straight, symmetrical airfoil blades. Cambered S818 airfoil blades display better self-starting characteristics at most azimuthal angles, and Savonius rotors provide the best start-up performance. In order to achieve a completely self-starting rotor at all azimuthal positions, a hybrid system was modeled. The H-Savonius rotor contained a three-bladed cambered Darrieus rotor with a Savonius rotor as its starter. Self-starting capability was determined by positive static torque coefficient values at all angles. The model was then fabricated and tested in a wind tunnel at a range of Reynolds numbers. Five different overlap conditions were tested for the Savonius part of the rotor. Efficiency of the hybrid model was compared with a simple H-rotor. The optimum overlap ratio was found to be 0.15 at a tip speed ratio of 2.29 and Reynolds number of $1.29 \cdot 10^5$. The optimized hybrid model achieved a maximum power coefficient of 0.34 which resulted in a significant increase in power performance from the H-rotor only model. The hybrid H-Savonius model in this study provided better power performance than most existing VAWT rotors while possessing the ability to self-start (Bhuyan and Biswas 2014).

2.11 Experimental testing

Experiments help to determine the effects of different rotor geometries on the torque and power coefficient of turbines. Once a numerical investigation has provided insight on a particular turbine, an experiment should be designed to validate the results. Rui-Tao et al (2011) developed a simple wind tunnel specifically for VAWT testing. The straight-flow wind tunnel test equipment information was made available to those who wish to verify numerical simulations through experimentation.

2.12 Computational Fluid Dynamic (CFD) approaches

CFD simulations combined with experimental studies provide the most informative results for VAWT research. CFD approach is an inexpensive method for predicting performance prior to fabricating models. Also, it can play a crucial role in identifying optimum design parameters. According to Islam et al (2008), the best numerical models validated for VAWT computations fell into three categories. The three categories were momentum model, vortex model, and cascade model. Each of these had specific advantages and disadvantages, but it was concluded that the cascade model gave smooth convergence at higher tip-speed ratios with reasonable accuracy. For drag-type rotors, Pope et al (2011) presented a new correlation for performance analysis. The correlation predicted power coefficient in terms of dimensionless numbers and specific turbine geometries. The robust correlation was extended to various rotor geometries. This CFD technique proved to be a useful design tool for improving Savonius VAWTs.

Recently, Alaimo et al. (2015) completed an analysis of VAWTs with computational fluid dynamics (CFD) using ANSYS Fluent software. The goal of the study was to compare performance of straight and helical shape turbines. The authors used two-dimensional and three-dimensional approaches to solve the Reynolds Averaged Navier-Stokes (RANS) equations. Two-dimensional simulations were used to approximate performance parameters such as torque, power, lift, and drag coefficients. Three-dimensional simulations were then carried out for a more accurate determination of aerodynamic properties of the complex geometries associated with helical blades. Static and dynamic numerical results were presented. Also, the accuracy and feasibility of different CFD approaches for VAWT investigation were described. Ultimately, tetrahedral elements were used to characterize the mesh, and the solution model was set using the
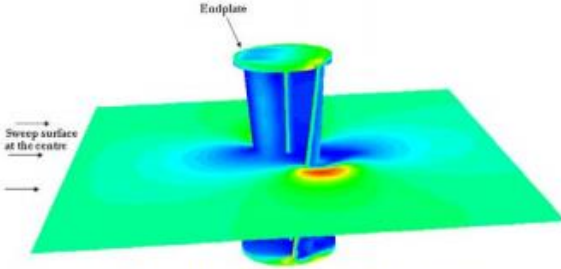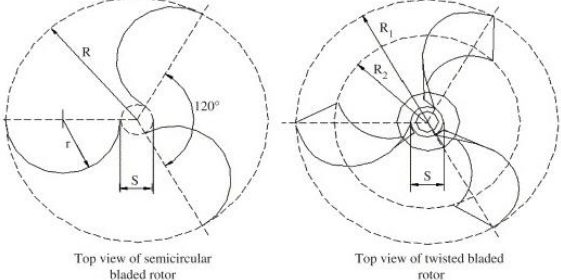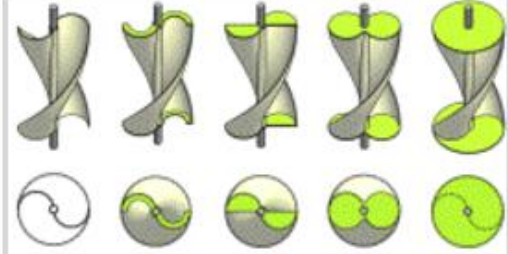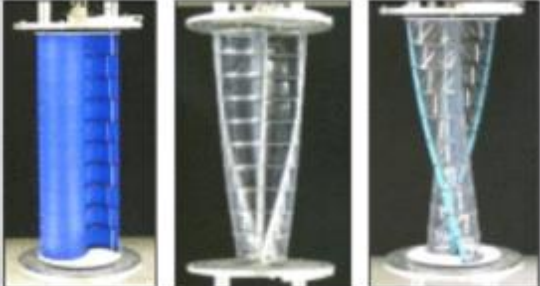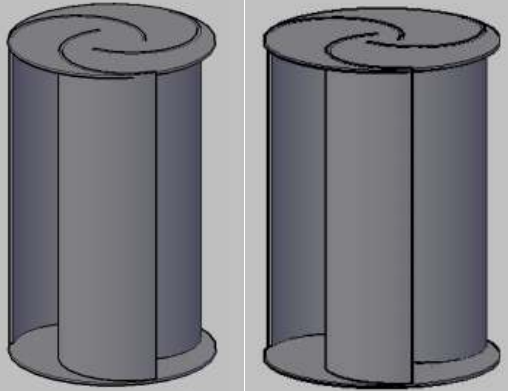
least-squares cell-based option with second order interpolation for face pressure. The realizable k-epsilon turbulence model is the recommended two equation turbulence model to account for rotation and strain in the flow (Sagol, Reggio and Ilinca (2012). For dynamic simulations, a moving reference frame solution should serve as the initial condition for the sliding mesh calculation (FLUENT Manual 2012).
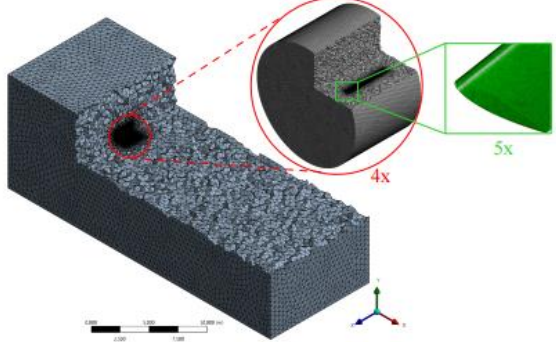
2.13 Summary of theoretical framework

A summary of the author works and key findings which led to the framework of the research presented in this thesis is displayed in Table 2.1.

Table 2.1. Summary of VAWT research

Researcher(s)	Studied	Findings	Figure
Wenehenubun et al. (2015)	Influence of increasing number of blades on Savonius rotor	4 blade turbine performs best at low tip-speed ratios, 3 blade at higher tip-speed ratios	
Ghatage et al. (2012)	Effects of twisted rotors	Twisting the blades enhanced efficiency of turbine	None
Can et al. (2013)	2 blade helical rotor vs. S-blade (Savonius)	Savonius rotor produces neg. torque coefficient in 2 ranges of operation, while helical does not	

Bachu, Gupta, and Misra (2013)	Helical rotor with 45° twist angle	Significant power increase at rotor angle 90° respect to incoming air velocity	 Fig. 5 Sweep surface at centre X=0, Y=1, Z=0
Saha and Rajkumar (2006)	Varied twist angle	Larger twist angle recommended for lower wind velocities	
Jeon et al.	End plate size and geometry on 180° twist helical VAWTs	Circular end plates top and bottom increased power coefficient by 36%	
Ricci et al. (2016)	Different configurations for Savonius turbines	Maximum Cp with 105° helical twist, end plates, and central gap	
Morshed, Rahman, and Ahmed (2013)	2D numerical simulation of different overlap ratios for 3 blade Savonius	Highest torque coefficient achieved with 0.12 overlap ratio	

Alaimo et al. (2015)	Development of 3D simulation for helical VAWTs	Tetrahedral elements used to characterize the mesh, second order interpolation for face pressure	
Sagol, Reggio, and Ilinca (2012)	Turbulence models for VAWT simulation	Realizable k-epsilon is recommended to account for flow rotation and strain	None

2.14 Motivation for research

Based on the literature review, some gaps in the VAWT research are identified. First, only semi-circle geometries are used for Savonius blades. Second, there is no available data for helical models with 90 degree twist angle, even though positive results are seen with higher twist angles in low TSR ranges. Also, there is plenty of research involving changing the number of blades for standard Savonius turbines but none for varying blade number of helical models. Lastly, very few researchers have developed three-dimensional and transient flow simulations for the study of aerodynamic behavior of vertical-axis wind turbines. With these opportunities for advancing the body of knowledge in mind, the following goals are outlined for this thesis:

- Improve the existing subsonic wind tunnel by fabricating a new model test section
- Model 3 Savonius blade geometries in SolidWorks with different cross-section geometries
- Validate increased performance of new designs with numerical simulations
- Complete CAD models of helical designs with 2-4 blades
- 3D print 6 models for experimental testing

- Design and implement new test fixtures to accompany 3D printed turbines

- Experimentally determine the self-starting capabilities and power coefficients of the 6 VAWT models (wind velocity, RPM, torque)

- Investigate performance of helical models with ANSYS Fluent simulation and plot power coefficient vs. tip-speed ratio

CHAPTER 3

METHODOLOGY

3.1 Introduction

This section of the thesis covers procedures for the experimental and numerical studies. An open-type, subsonic wind tunnel is used for the experimental portion of this study. At each wind speed tested, reactional torque, wind velocity, and RPM data are collected. Reactional (static) torque is measured for every 10 degrees of turbine rotation. ANSYS Fluent software is used for computational fluid dynamics simulations. The simulations are performed in three dimensions to gather moment coefficient data over time for one rotation.

3.2 Model design and fabrication

In total, six different VAWT models are tested in the study. Each model is developed using SolidWorks commercial CAD software. Due to some complex and twisted geometries, the models are 3D printed using fused deposition modeling (FDM) and stereolithography (SLA) methods. The models are named SAV, CC, QM, Helical2, Helical3, and Helical4 for reference. The traditional Savonius model with straight blades, SAV, is used for benchmarking and comparing results of the new designs. The SAV cross-section can be seen in Figure 3.1.
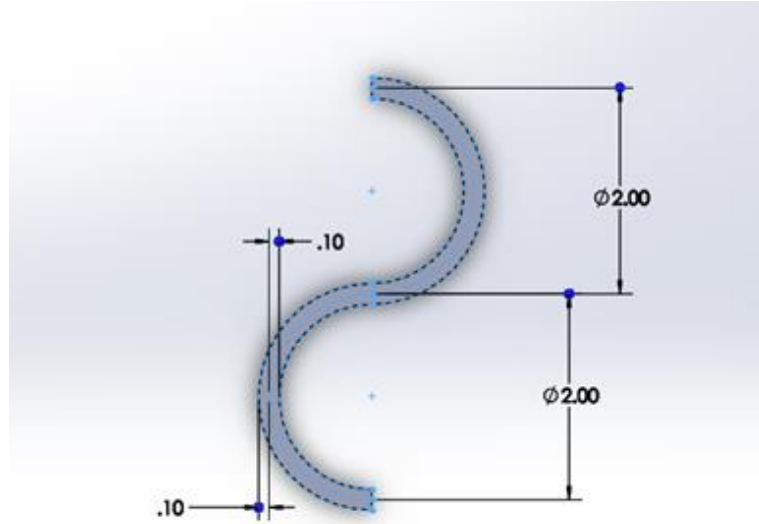
Figure 3.1. SAV model cross-section

Each model in the study is designed with a 4.2 inch blade diameter (*D*) and blade height (*H*) of 4

inches; therefore, the swept area (*A*) is kept consistent across all models. Cross-sectional views

of the new Savonius designs, "CC" model and "QM" model, are displayed in Figure 3.2.
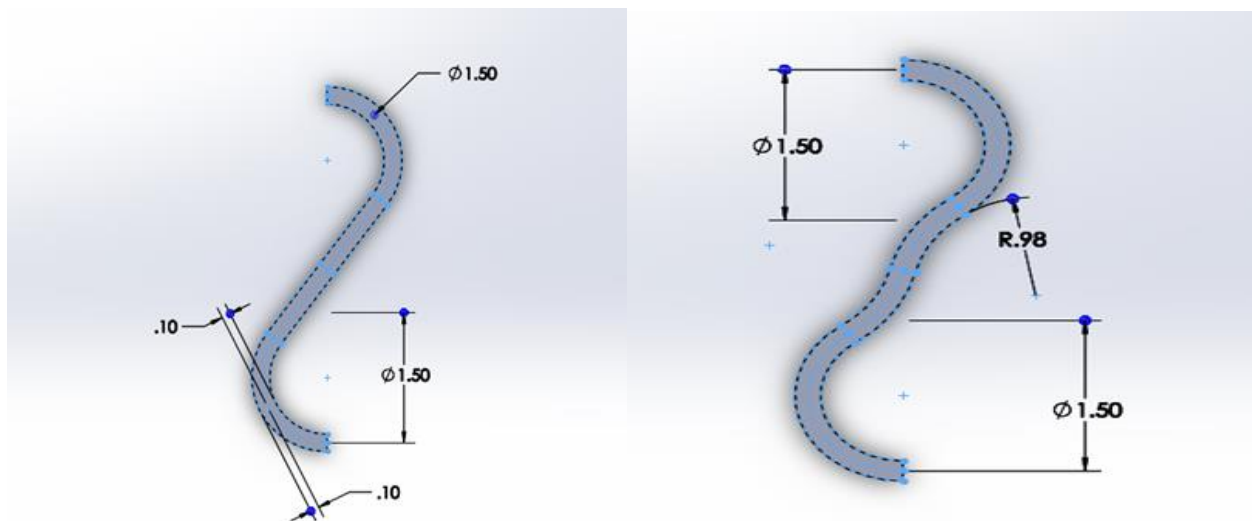
Figure 3.2. CC model (left) and QM model (right) cross-sectional views with dimensions

CC is modeled with slightly smaller diameter buckets of 1.5 inches, connected with a tangent

line. The QM model has the same dimensions with a curved line connecting the 2 blades. The

idea for these new models is to create a center of pressure further from the axis of rotation, causing greater torque on the turbine shaft. The SLA 3D printed models are presented in Figure 3.3.

Figure 3.3. SLA 3D printed models

The other three VAWT models in the study are constructed with a helical twist of 90 degrees. Helical2, Helical3, and Helical4 have similar cross-sections to that of the traditional Savonius with varying number of blades from 2 to 4. Details of the blade-tip helix for each of these models may be seen in Figure 3.4.
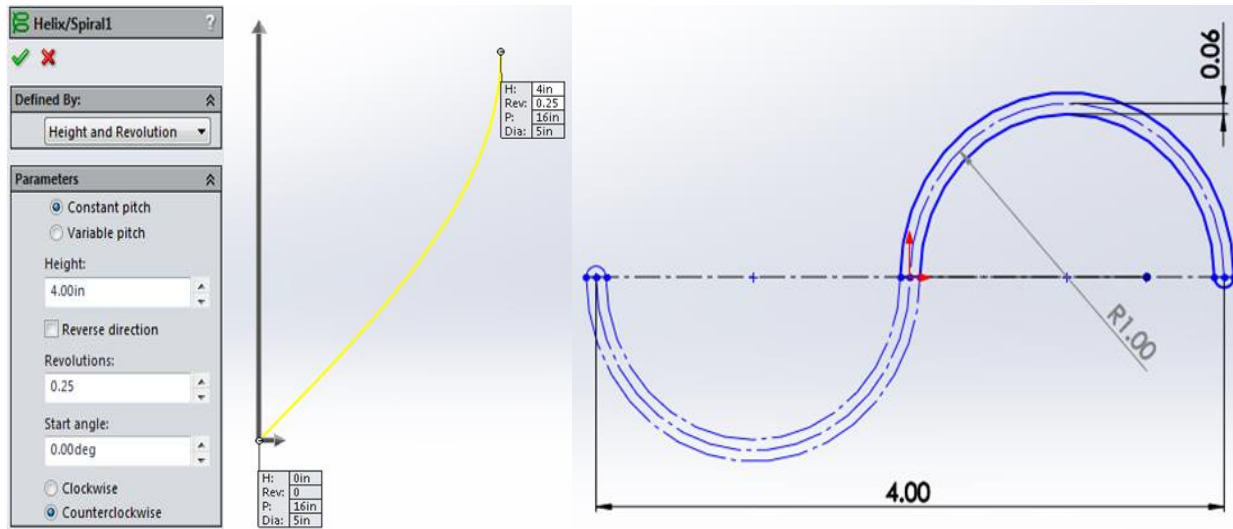
Figure 3.4. Details of 90 degree twist used for helical models

Completed CAD models of the VAWTs with 90 degree helical twist may be seen in Figure 3.5.

Pictured from left to right, these models are Helical2, Helical3, and Helical4. The helical models

spread torque values more evenly over a full rotation, resulting in positive torque coefficients for

all operating angles.
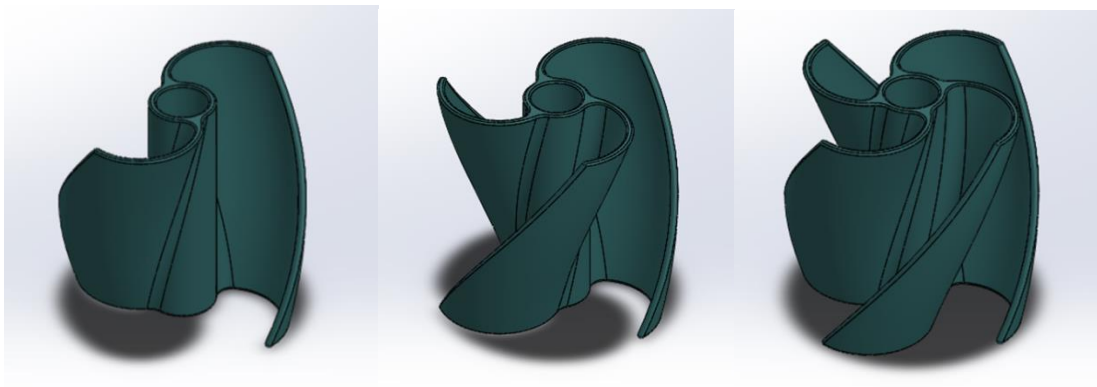
Figure 3.5. CAD models of Helical2, Helical3, and Helical4 (from left to right)

These physical models are then created from PLA plastic with a FDM 3D printer for

experimental testing, shown in Figure 3.6.

Figure 3.6. FDM 3D printed helical models

3.3 Experimental set-up and equipment

The Georgia Southern wind energy laboratory is equipped with a subsonic open-type wind tunnel for experimental testing. The existing wind tunnel and test section are shown in Figure 3.7 and the sections are shown in Figure 3.8. The wind tunnel inlet is shown in the far left of the photo, followed by a honeycomb section for laminar flow. The fan is controlled by a Huanyang variable frequency drive. Another honeycomb section immediately follows the fan. Next is a diverging-converging section with a 9 to 1 area ratio to the 2 ft. by 2 ft. wind tunnel outlet. The VAWT test section frame is also showed at the wind tunnel outlet. As part of this research, a new test section is created for large VAWTs and future HAWT experiments.

Figure 3.7. Existing wind tunnel configuration
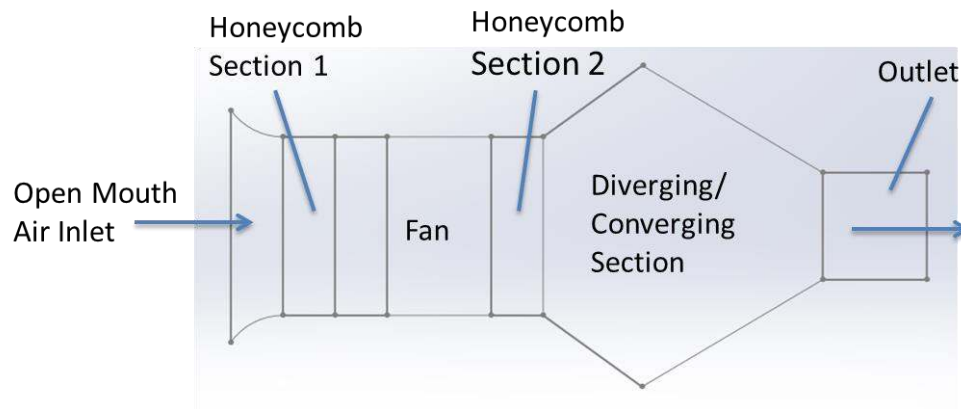
Figure 3.8. Wind tunnel sections schematic

3.4 New test section design

In order to test large models within the walls of the wind tunnel and with more laminar flow around the blades, a new model test section is designed and fabricated. Detailed steps and fabrication procedures for the test section can be viewed in Appendix B. This work is further described in a paper published by the author entitled "Experimental Set-up Design and Testing of Vertical and Horizontal Axis Wind Turbine Models in a Subsonic Wind Tunnel." The new test section is capable of containing larger VAWT models and HAWTs as well. It is equipped with acrylic doors for full visibility while testing models inside the tunnel. The doors also allow for

easy installation and replacement of several different prototypes. The completed assembly is shown in Figure 3.9.

Figure 3.9. Completed assembly of new wind tunnel test section

CFD results are used to determine proper configuration of the new test section within the existing wind tunnel. Based on the simulations it is determined that the most suitable placement for the new section is at the end of tunnel. At maximum power in this configuration, the old outlet acts as a nozzle producing a uniform 11 m/s velocity through the start of the test section. A diffuser is used to connect the old outlet with the new section flange. This configuration allows for easy removal of the test section in case researchers wish to test smaller models with the old, smaller tunnel outlet. CFD results for existing and new tunnel configuration are presented in Figures 3.10 and 3.11, respectively.
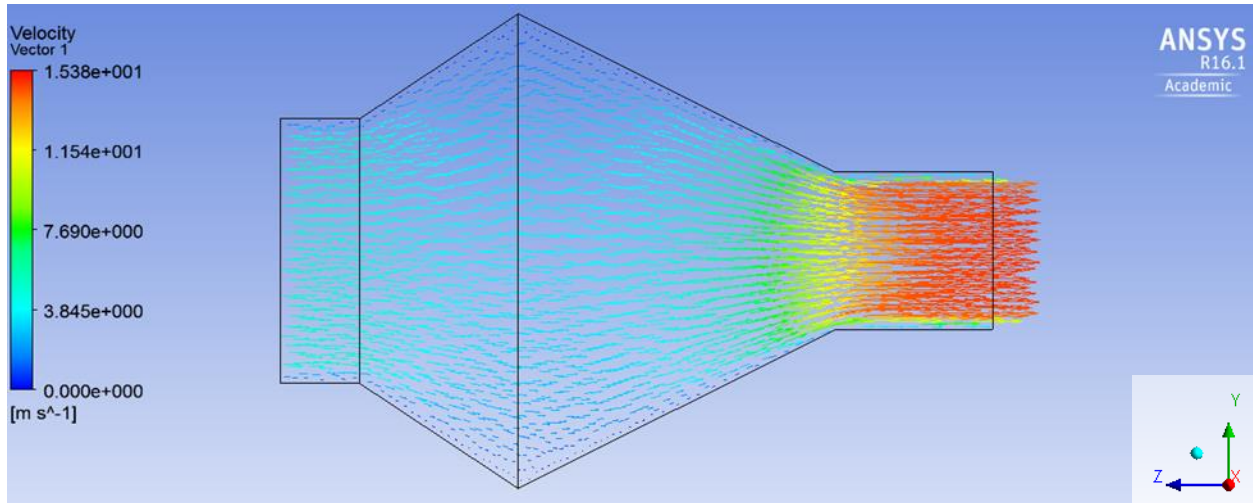
Figure 3.10. Existing wind tunnel configuration
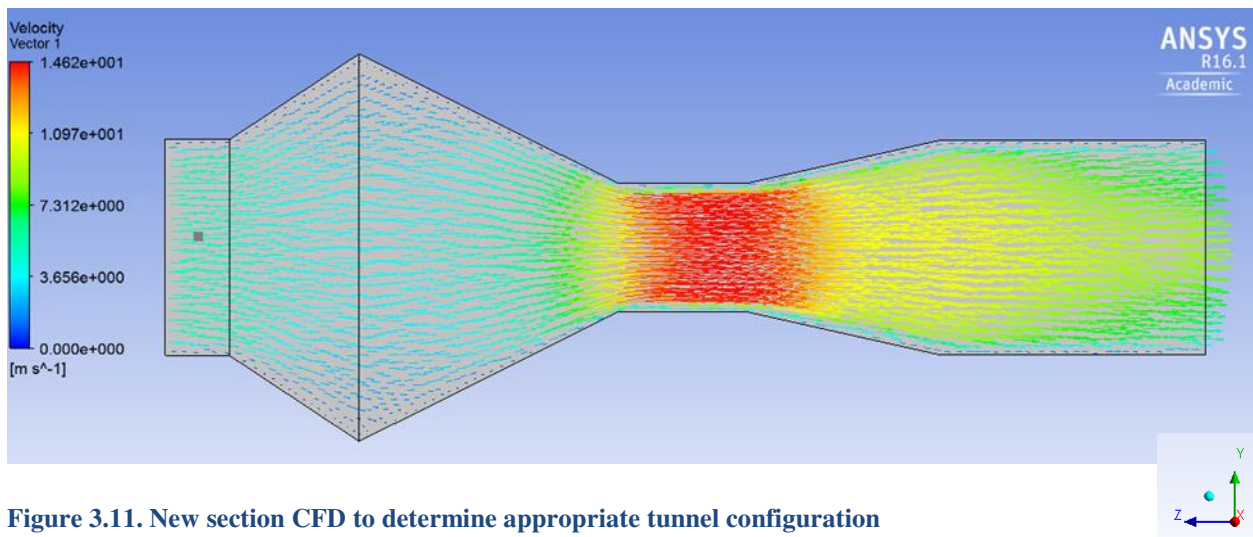
Figure 3.11. New section CFD to determine appropriate tunnel configuration

3.5 Wind velocity

Free stream velocity through the test section is easily controlled with the variable frequency drive (VFD) operator interface shown in Figure 3.12. Consistent and maintainable RPMs of the motor depend on the frequency, measured and displayed in Hertz, transmitted from the VFD. The internal fan produces wind speeds of 0 to 13 m/s through the outlet.

Figure 3.12. Huanyang variable frequency drive operator interface

A hand held anemometer, displayed in Figure 3.13, is used to measure wind velocity for each test. Wind speed is measured about 6 inches in front of the model and centered on the axis of rotation. The instrument is capable of measuring current, maximum, or average wind speed. Each time the VFD is used to alter wind conditions, current wind speed is measured in time intervals of 2-10 seconds. For each experiment at a given wind speed, 5 separate readings of current wind velocity are taken to ensure consistent wind conditions. The anemometer has a range of 0.2 to 30 m/s and is accurate to 0.1 m/s.

Figure 3.13. Hand held anemometer for wind velocity measurement

3.6 RPM measurement

A small circular base with 2.5 in. vertical shaft is used for RPM measurement. Two sealed stainless steel ball bearings are fitted inside the models to allow for free rotation on the fixed shaft. The fixture and bearings can be seen in Figure 3.14.
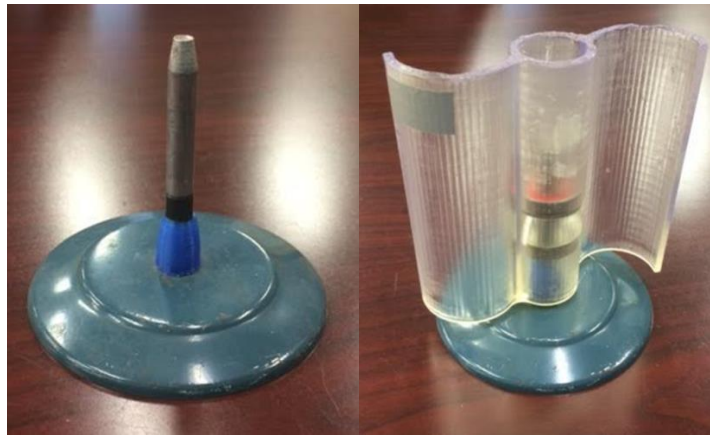
Figure 3.14. RPM measurement fixture (left) and CM model with bearings (right)

A laser tachometer is used to measure RPM of the models under varying wind conditions, seen in Figure 3.15. A small piece of reflective tape is applied to the top of one blade to reflect the infrared light. A detector on the tachometer receives the reflected light and detects changes in frequency. The frequency change over time gives the rotational speed of the VAWT models.
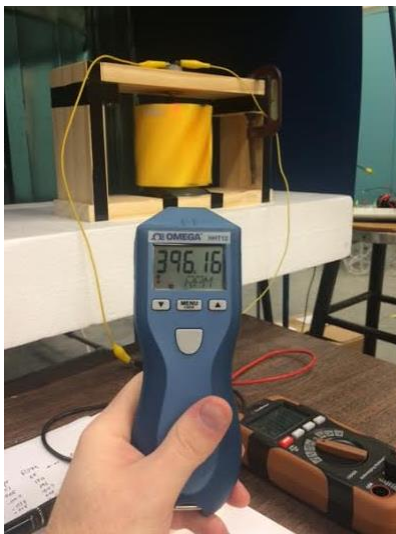
Figure 3.15. Laser tachometer for RPM measurement

3.7 Torque measurement

A reactional torque meter is used for each model under increasing wind speeds. For each wind condition, torque is measured at every 10 degrees of turbine rotation. The torque meter and experimental setup is displayed in Figure 3.16.
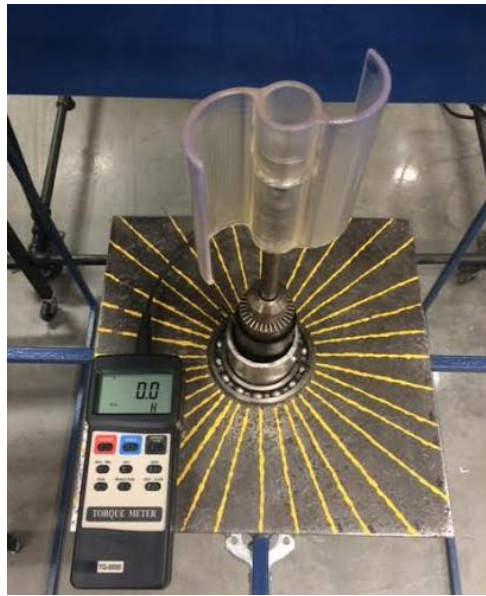
Figure 3.16. The reactional torque meter and experimental setup

The torque meter used for experimentation is calibrated with a dial torque wrench, shown in Figure 3.17.

Figure 3.17. Dial torque wrench for torque measurement calibration

The base plate of the torque measurement fixture is marked for every 10 degrees of rotation. It is important to define the turbine angle relative to incoming wind velocity. The CC and Helical2

models are positioned on the fixture at an angle of zero degrees relative to incoming wind in Figure 3.18. A 10 degree clockwise rotation is equal to a position angle of 10 degrees. This definition of turbine angle relative to incoming wind is consistent throughout the research.
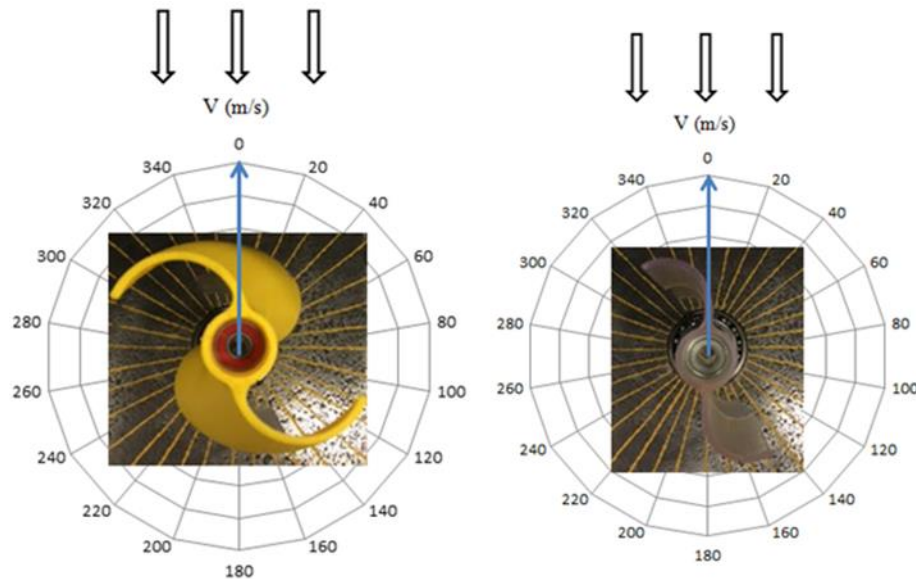
Figure 3.18. Helical2 (left) and CC (right) at 0 degree angle relative to incoming wind

3.8 Analysis

Once torque data is calculated, analysis must be done to compare the performance of the models to other research. Non-dimensional coefficients are used for comparison to other similar research and validation of the experiment. Three of these universally used non-dimensional entities are considered for this study. The power coefficient describes the energy conversion efficiency of the turbine. Torque coefficient is a non-dimensional representation of rotor torque, which is proportional to power produced. Tip-speed ratio is defined as the ratio of the blade tip speed to the free-stream wind velocity (MacPhee, David, and Beyene 2012).

Using the following equations, tip-speed ratio and moment coefficient data are used to calculate the power coefficient over a range of wind velocities for each heical rotor design [17].

In order to find the moment coefficient for each turbine, the rotor swept area must first be calculated using equation (1),

$$A = DH \tag{1}$$

where H is rotor height in m and D is overall diameter in m. A swept area schematic is shown in Figure 3.19 for the Helical2 model.
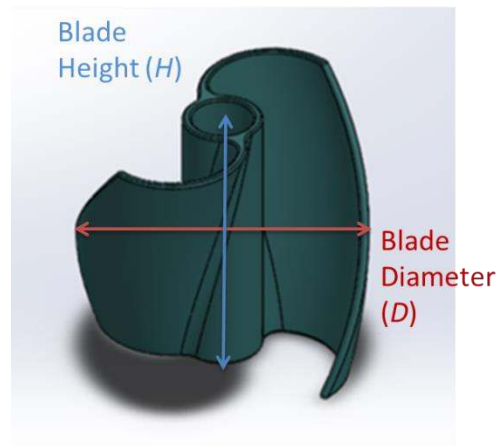
Figure 3.19. Swept area schematic

The swept area is kept consistent across all three models and used as a reference value in ANSYS Fluent for solving moment coefficients. The non-dimensional moment coefficient is calculated using equation (2),

$$C_m = \frac{T}{\frac{1}{4}\rho A D V^2} \tag{2}$$

where T is torque in $N \cdot m$, ρ is air density in $\frac{kg}{m^3}$, A is rotor area in m^2, and V is air velocity in $\frac{m}{s^2}$. The non-dimensional term for comparing efficiency of VAWTs is the power coefficient. First the angular velocity of the rotor must be calculated by equation (3),

$$\omega = \frac{2\pi N}{60} \qquad (3)$$

where N is the measured revolutions per minute. Once the angular velocity is determined, the tip-speed ratio of the rotor is solved from equation (4).

$$\lambda = \frac{\omega D}{2V} \qquad (4)$$

The power coefficient is then calculated. As can be seen by equation (5), the power coefficient is found from the product of tip-speed ratio and moment coefficient.

$$C_p = \frac{P}{\frac{1}{2}\rho AV^3} = \frac{T\omega}{\frac{1}{2}\rho AV^3} = \lambda Cm \qquad (5)$$

3.9 Numerical procedure

In order to understand the pressure distributions and aerodynamic characteristics of the various blades in the study, numerical simulations are performed using commercial CFD software ANSYS Fluent. The CAD models are imported into ANSYS DesignModeler, and fluid regions are added to the geometry. For transient three-dimensional analysis of VAWTs, two separate fluid domains are needed for simulation (Alaimo et al. 2015). A 9 inch diameter

spherical enclosure around the model is used for a rotating zone. A second, stationary zone is created with a uniform box enclosure as the far-field domain. The entire three-dimensional computational domain is displayed in Figure 3.20.
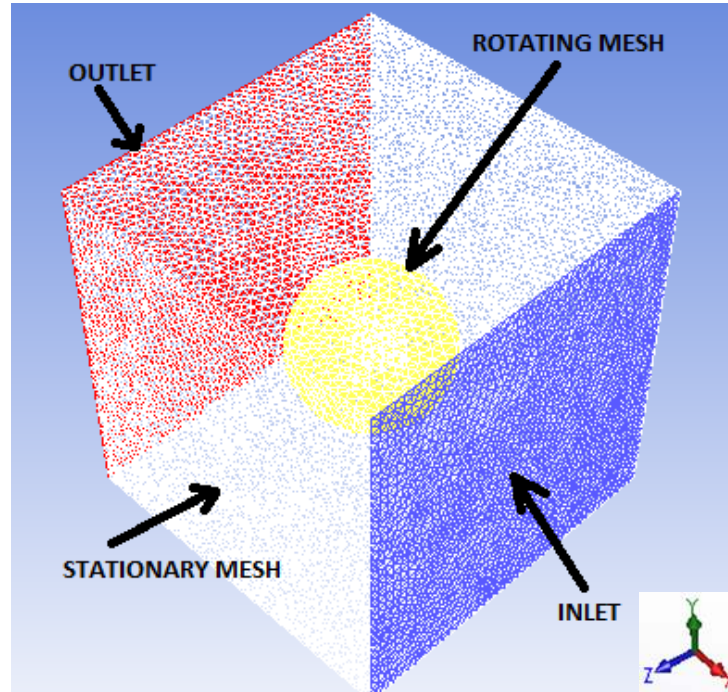
Figure 3.20. Three-dimensional computational domain

The fluid domains are discretized using ANSYS Meshing. Each mesh consists of around 500,000 tetrahedral elements since the maximum allowable number of cells for ANSYS Fluent Academic is 512,000. The number of elements and nodes for each mesh are given in Table 1.

Table 3.1. Number of three-dimensional mesh elements and nodes

	Savonius	CC	QM	Helical2	Helical3	Helical4
Elements	503,727	453,849	495,219	501,394	502,216	506,989
Nodes	92,986	85,320	88,663	89,656	89,754	90,557

An example mesh is displayed in Figure 3.21. A top view of wireframe mesh is shown on the left, and a sectional view displaying the two separate cell zones is on the right.
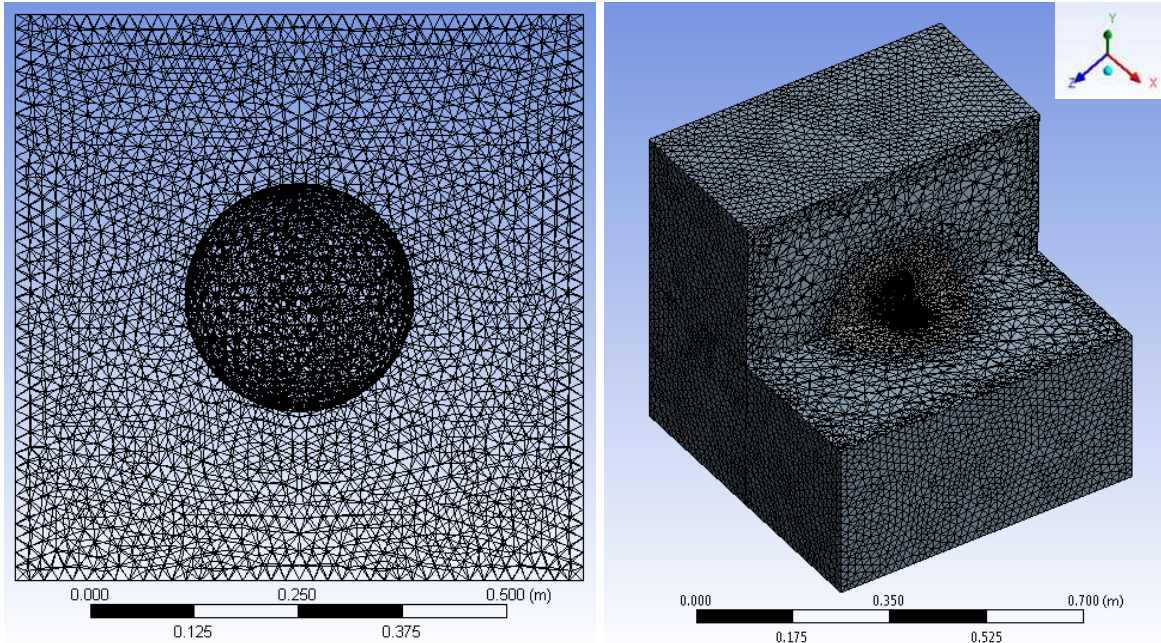
Figure 3.21. Top view of Savonius model mesh (left) and sectional view (right)

The realizable k-epsilon turbulence model with standard wall functions is used for each solution. The realizable model is comparable to the RNG model with more accurate solutions where the flow features include vortices and rotation; however, studies have shown that the realizable model provides the best performance of all k-epsilon models for several validations of separated flows and flows with complex secondary flow features (FLUENT Manual 2012).

As discussed, the computational domain consists of a rotating zone surrounding the blades and a stationary far-field zone. A mesh interface is created between the two zones. The interface is necessary because the nodes on the boundaries of the far-field and rotational zones are intentionally non-conformal. The interface pairs these so that interpolation can occur, and fluid may pass into and out of the rotating region. For each case, a static simulation with moving reference frame (MRF) and a dynamic sliding mesh model (SMM) are completed. The rotation is first defined using the steady-state solver with MRF, and the simulation is then solved in a

transient manner using a sliding mesh motion. The converged static result from the MRF simulation is used to initialize the transient SMM solver. Example graphs of the residuals for MRF and SMM simulations can be seen in Figure 3.22. Convergence criteria are kept consistent throughout the study requiring all 5 residuals to decrease to a value of 1e-03.
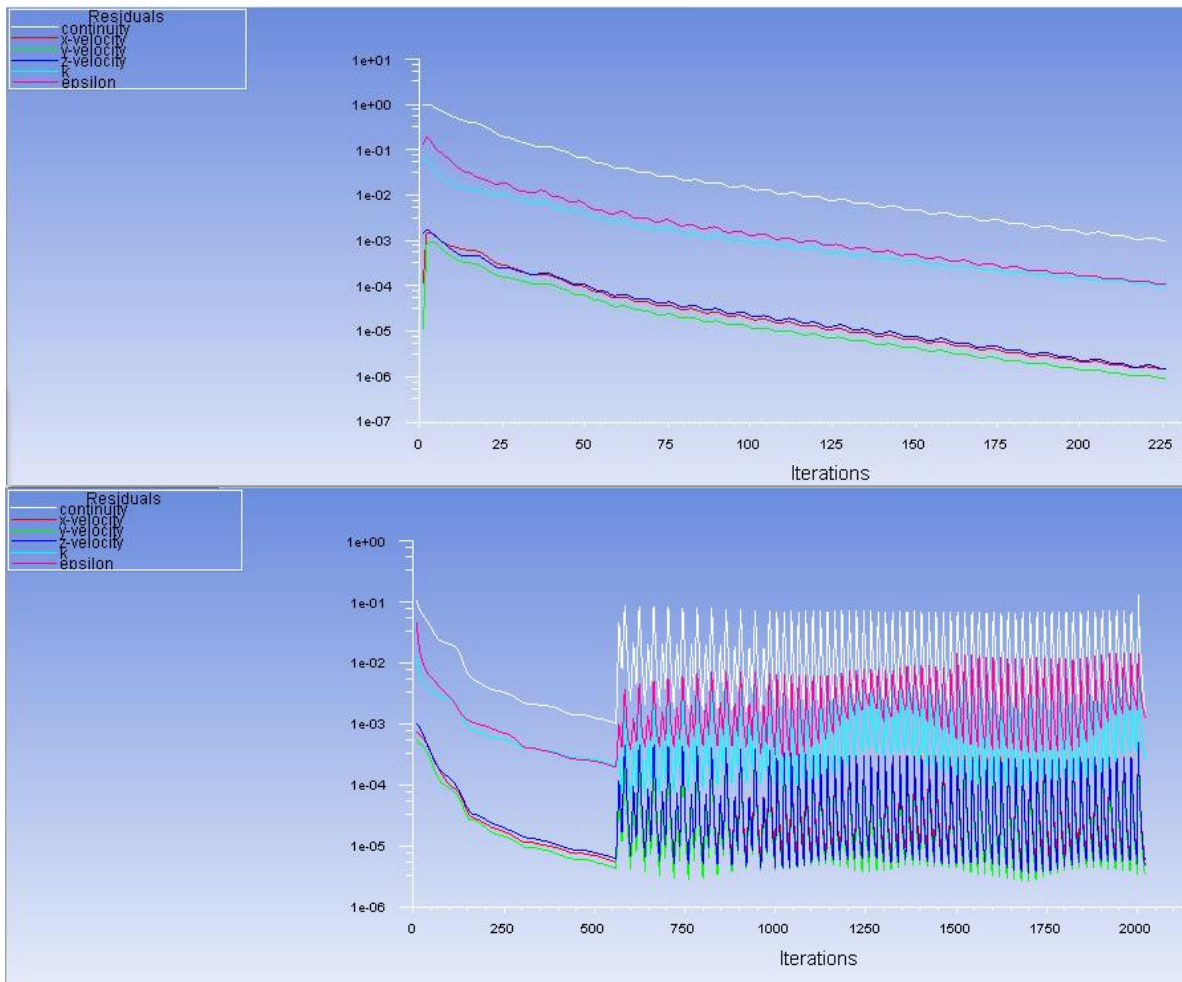
Figure 3.22. MRF residuals converged after 225 iterations and SMM residuals

For the transient solver, coefficients of moment (*Cm*) are monitored over time with accurate reference values. Time step size is dependent on the RPM value for each case. Time steps are calculated to account for every 10 degrees of model rotation. For 2 full rotations, 72 time steps per simulation are run with 20 iterations per time step.

3.10 Boundary Conditions

Boundary conditions for the simulations are taken from experimental data. These include air velocity inlet speed and corresponding rotational speed of the blades. The pressure outlet is kept at constant atmospheric pressure. The blade walls are given a no slip condition and zero rotational velocity relative to the sliding mesh zone (equal to the rotating fluid domain).

3.11 Turbulence Model

The realizable k-epsilon model is used with the SIMPLE segregated algorithm. The SIMPLE algorithm uses a relationship between velocity and pressure corrections to enforce mass conservation and to obtain the pressure field (ANSYS Fluent Theory Guide, 2012). For improved accuracy, the double precision option is selected as well as second order upwind based discretization for mean flow, turbulence, and transition equations. The turbulence kinetic energy (k) and its dissipation rate (epsilon) for the realizable k-epsilon model are obtained from the following transport equations:

$$\frac{\partial}{\partial t}(\rho k) + \frac{\partial}{\partial x_j}(\rho k u_j) = \frac{\partial}{\partial x_j}\left[\left(\mu + \frac{\mu_t}{\sigma_k}\right)\frac{\partial k}{\partial x_j}\right] + P_k + P_b - \rho\epsilon - Y_M + S_k$$

and

$$\frac{\partial}{\partial t}(\rho\epsilon) + \frac{\partial}{\partial x_j}(\rho\epsilon u_j) = \frac{\partial}{\partial x_j}\left[\left(\mu + \frac{\mu_t}{\sigma_\epsilon}\right)\frac{\partial\epsilon}{\partial x_j}\right] + \rho\,C_1 S\epsilon - \rho\,C_2\frac{\epsilon^2}{k + \sqrt{\nu\epsilon}} + C_{1\epsilon}\frac{\epsilon}{k}C_{3\epsilon}P_b + S_\epsilon$$

where

$$C_1 = \max\left[0.43, \frac{\eta}{\eta + 5}\right], \quad \eta = S\frac{k}{\epsilon}, \quad S = \sqrt{2S_{ij}S_{ij}}$$

In these equations, P_K represents generation of turbulence kinetic energy due to mean velocity gradients, and P_b is generation of turbulence kinetic energy due to buoyancy (ANSYS Fluent Theory Guide, 2012).

CHAPTER 4

FINDINGS OF THE STUDY

4.1 Introduction

This chapter covers the results and discussion of all numerical and experimental analysis carried out in the research. The information is organized as follows:

- First, simulations are carried out with varying wind conditions and constant rotational speed to verify that the new blade geometries, CC and QM, produce greater torque than the traditional SAV model.

- Self-starting characteristics of all 6 models are investigated with wind tunnel testing and no load conditions.

- Experimental torque is recorded for all models in varying wind conditions. The data is used to present corresponding torque and power coefficients.

- 3D Numerical simulations with input boundary conditions from experimental data are conducted. Coefficient of moment is recorded for each simulation and used for determining efficiency of each turbine. Results are discussed and compared to the wind tunnel experiments.

4.2 Initial simulations of straight-bladed models

Prior to completion of the wind tunnel improvements and fixtures for experimental testing, some numerical simulations are performed to verify concepts. A 3D CFD analysis is conducted for the SAV, CC, and QM models to study the effects of the different geometries on the amount of torque generated. Rotational speed of the models is kept constant at 275 RPM for all models and all tip-speed ratios (TSRs) in this part of the study. Only inlet velocity is varied with speeds of 3, 5, and 7 m/s. The increasing wind speeds resulted in tip-speed ratios of 0.51,

0.31, and 0.22. The following results contain the transient moment coefficient monitors for the simulations with constant rotational speed.

The SAV model is used for obtaining baseline results, to which the new designs may be compared. At 3m/s inlet velocity, the maximum *Cm* is 0.134 with an average of 0.029. At 5 m/s the maximum *Cm* is 0.560 with an average of 0.145. At 7m/s the maximum *Cm* is 1.248 with an average of 0.315. The *Cm* vs. time graph for SAV is displayed in Figure 4.1. At 7 m/s inlet velocity, the SAV model experiences negative torque in two ranges of operation: 0 - 55 degrees (0 - 0.039s) and 175 - 230 degrees (0.105 - 0.138s).
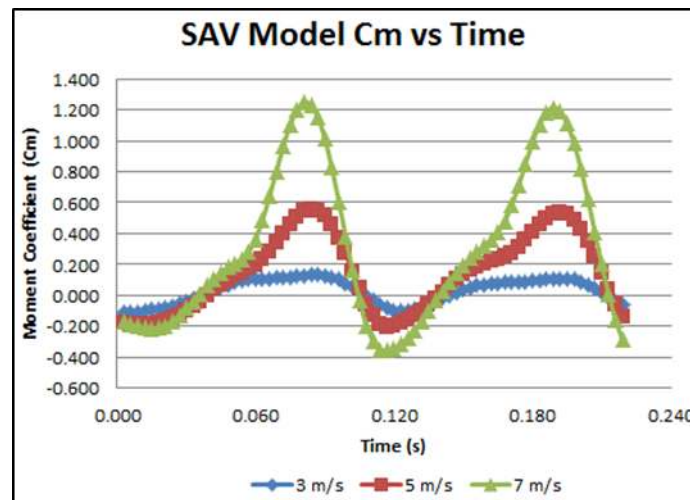
Figure 4.1. Transient monitor of moment coefficient (*Cm*) for SAV model with wind speeds of 3m/s, 5m/s, and 7m/s

The CC rotor experiences higher maximum and average moment coefficients than SAV at all 3 tested tip-speed ratios. The maximum *Cm* achieved is 1.390 at 7m/s inlet velocity. Results are displayed in Figure 4.2. At the maximum inlet velocity, the CC model also experiences negative torque in two ranges of operation: 5 - 45 degrees (0.003 - 0.027s) and 185 - 235 degrees (0.111 - 0.141s). The total range of negative torque at 7 m/s wind velocity is 20 degrees more narrow, compared to the SAV model.
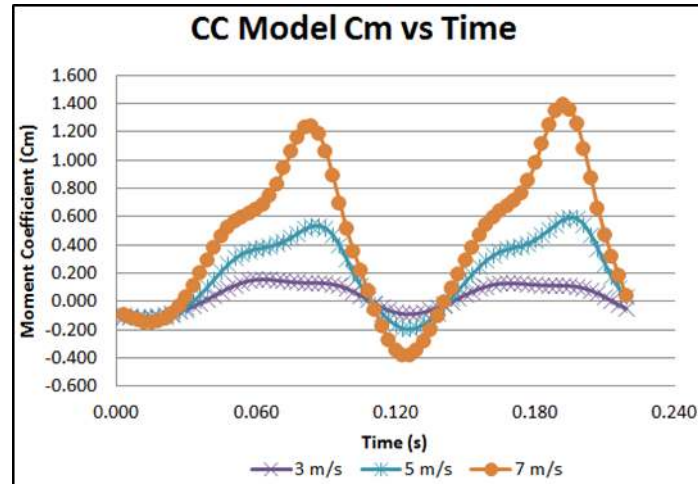
Figure 4.2. Transient monitor of moment coefficient (*Cm*) for CC model with wind speeds of 3m/s, 5m/s, and 7m/s

The QM model outperforms both the CC and SAV models in terms of maximum moment coefficient at 5 and 7m/s inlet velocities. At the highest tested TSR, QM enjoys the best performance in the constant RPM numerical study. With wind velocity set at 7m/s, QM achieves a maximum moment coefficient (*Cm*) of 1.474 with an average of 0.455. The range of negative torques at this inlet velocity is the same as that of the CC model: 5 - 45 degrees (0.003 - 0.027s) and 185 - 235 degrees (0.111 - 0.141s).
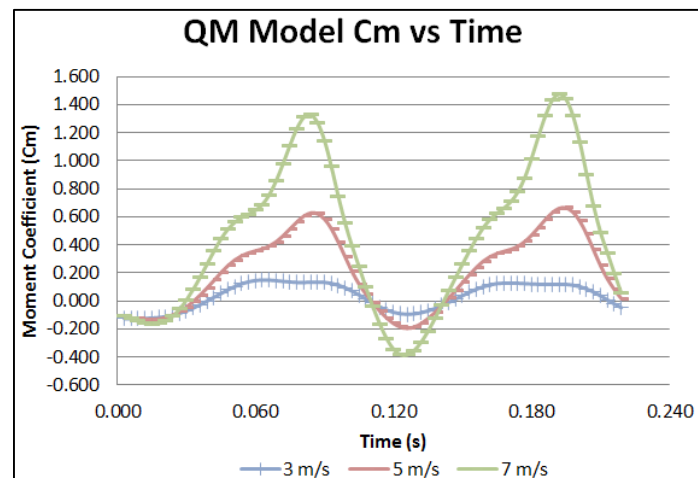
Figure 4.3. Transient monitor of moment coefficient (*Cm*) for QM model with wind speeds of 3m/s, 5m/s, and 7m/s

A comparison of *Cm* data for each design is presented in Figures 4.4 - 4.6 at inlet velocities of 3,

5, and 7m/s, respectively.
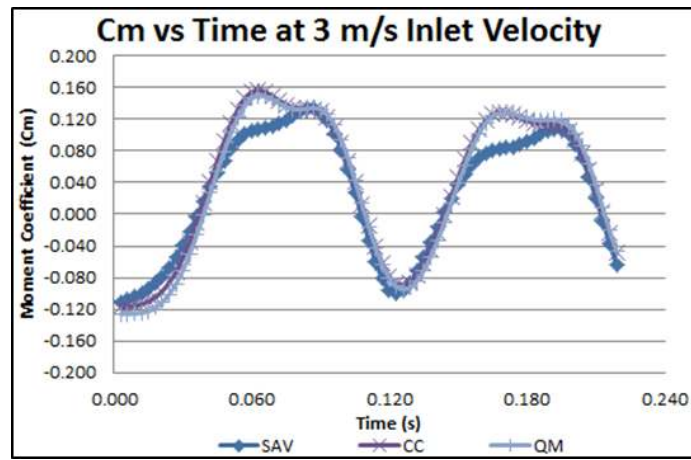
Figure 4.4. *Cm* **Comparison of 3 models at 3m/s inlet velocity**
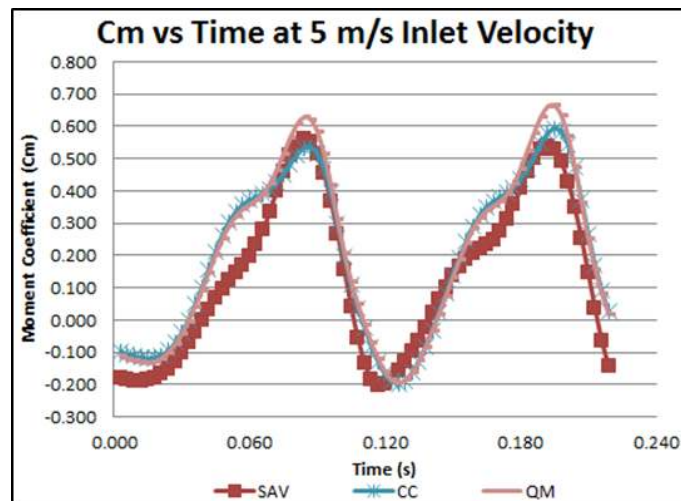
Figure 4.5. *Cm* **Comparison of 3 models at 5m/s inlet velocity**
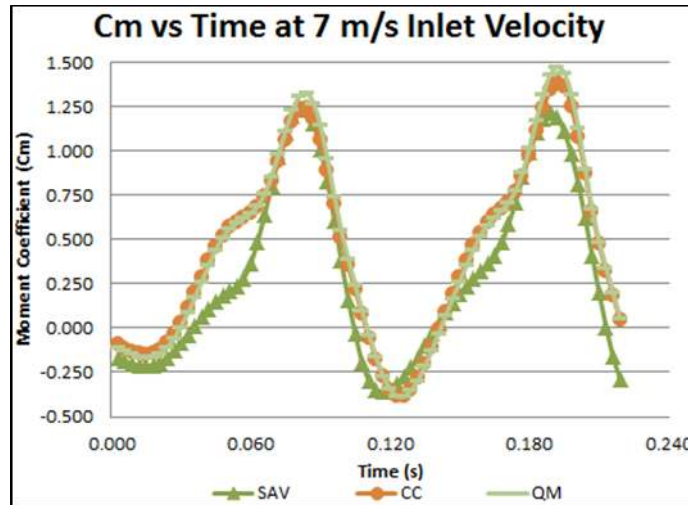
Figure 4.6. *Cm* **Comparison of 3 models at 7m/s inlet velocity**

At highest simulated wind speed, SAV experiences negative torque from 0-55 degrees and 180-235 degrees. QM and CC both have negative torque ranges of 5-45 degrees and 185-235 degrees. The new cross sections reduce the total range of negative torque by 20 degrees for one full rotation. As can be seen in the comparison figures, a large difference in moment coefficient between the new designs and the traditional SAV model occurs at about 0.06 seconds (100 degrees) for each tested wind speed. CFD post-processing within the ANSYS Fluent software is used to investigate the aerodynamic characteristics at this time step. Air pressure contours surrounding the blades, air velocity vectors, and blade wall pressures are displayed in Tables 4.1 – 4.3 for the 5m/s wind velocity simulations.

Table 4.1. Air pressure contours surrounding blades at 0.06s
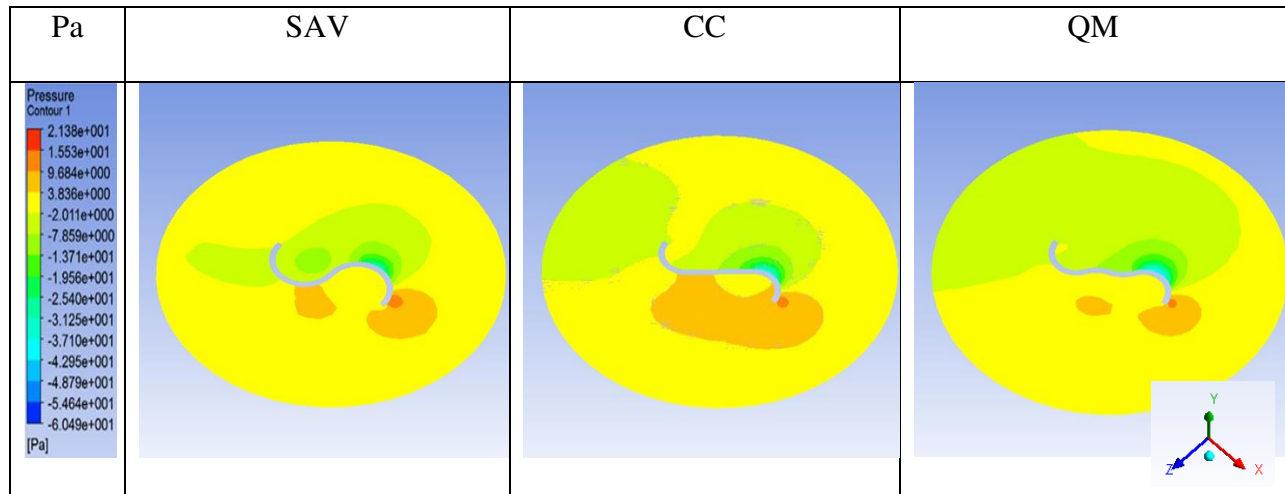
The SAV model experiences higher pressure at the front of the blades. CC and QM experience more negative pressure on the back side of the blade. These two conditions result in greater torque for the CC and QM models.

Table 4.2. Air velocity vectors surrounding blades at 0.06s
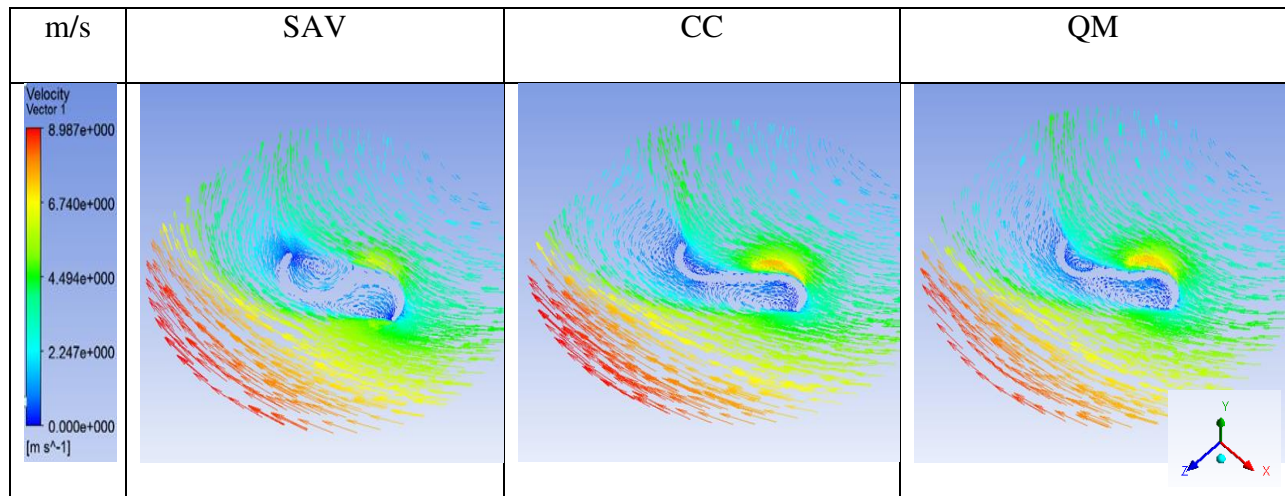
The air velocity vectors for each model are shown in Table 4.2. Compared to the SAV model, higher velocities are present on the back side of the retreating blade for the new designs. This results in a greater pressure difference and larger moment coefficient.

Table 4.3. Pressure contours on the backside of retreating blades at 0.06s
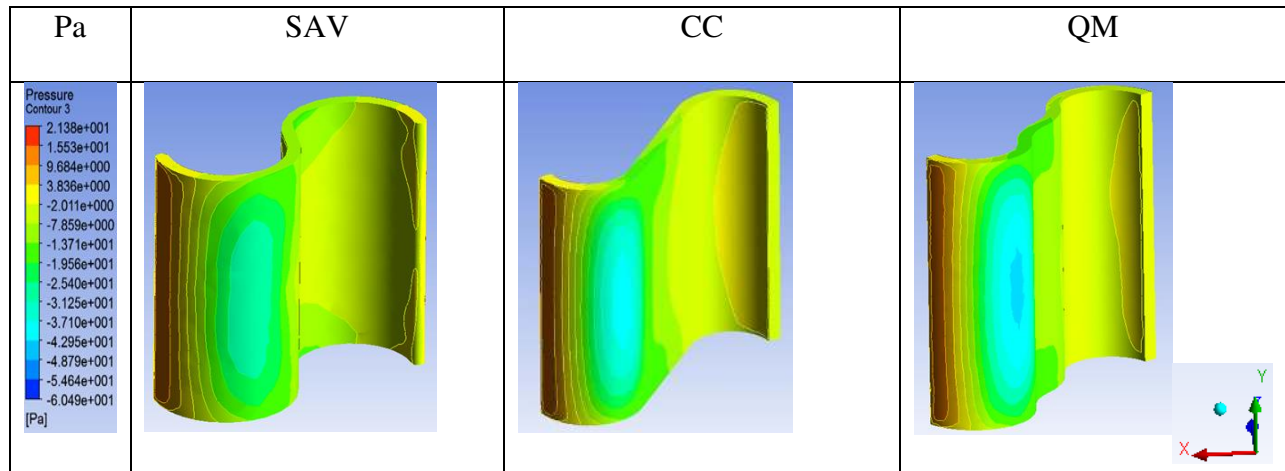
The negative pressures on the reverse side of the retreating blades at 0.06s are presented as 3D pressure contours in Table 4.3.

Using calculated tip-speed ratio and moment coefficient data from ANSYS, the power coefficient (Cp) of each case is determined. All simulation data for the initial numerical study is available in Tables 1E – 3E of Appendix E. Maximum and average power coefficients for the 9 dynamic simulations in this study are presented in Table 4.1.

Table 4.4. Average and maximum *Cp* results of 3 models for constant RPM numerical study

Model	V (m/s)	TSR	Avg *Cm*	Max *Cm*	Avg *Cp*	Max *Cp*
SAV	3	0.512	0.029	0.134	0.015	0.068
SAV	5	0.307	0.142	0.560	0.043	0.172
SAV	7	0.219	0.315	1.248	0.069	0.274
CC	3	0.512	0.041	0.157	0.021	0.080
CC	5	0.307	0.203	0.594	0.062	0.182
CC	7	0.219	0.442	1.390	0.097	0.305
QM	3	0.512	0.037	0.150	0.019	0.077
QM	5	0.307	0.214	0.664	0.066	0.204
QM	7	0.219	0.455	1.474	0.100	0.323

A graph of maximum *Cp* vs. TSR for the 3 models is displayed in Figure 4.7. For all 3 blade geometries, the highest efficiency is achieved at lower tip-speed ratios. This is expected

because RPM was kept constant even with increasing inlet wind velocities. This also explains the high values of power coefficient. Although these are not realistic operating conditions for these models, the results in this section are only used to compare the aerodynamic performance of the different blade geometries. Both of the new designs achieve higher power coefficients than the semicircle Savonius blade design. Compared to the SAV model, CC achieves an 11.38% increase in maximum efficiency and a 40.07% increase in average efficiency. The highest efficiency observed in the study of 32.35% was the QM model at TSR 0.219. This was an increase in power coefficient of 18.10%, compared to the standard SAV model.
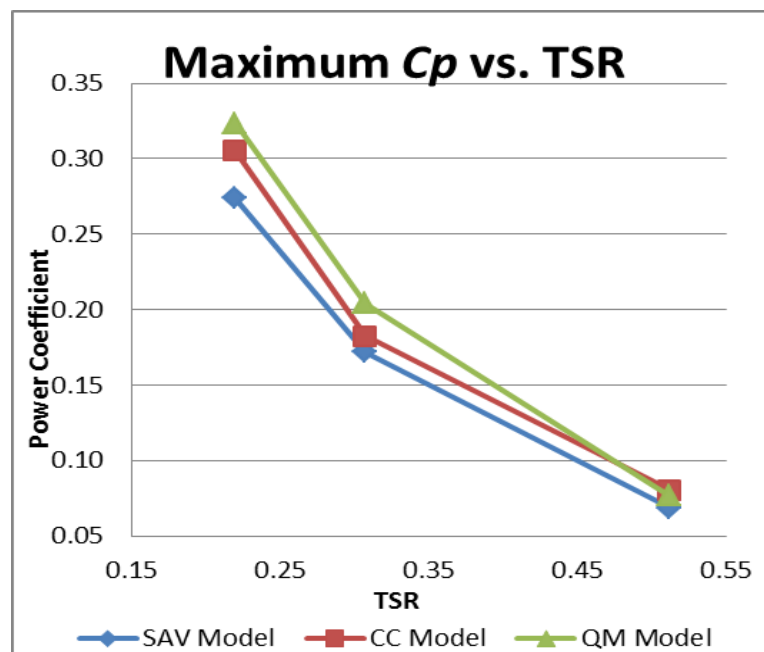
Figure 4.7. Max power coefficient vs. tip-speed ratio for 3 models in constant RPM study

Both QM and CC model geometries effectively produce a center of pressure on the blades further from the axis of rotation. This change in blade geometry increases the applied torque on the turbine shaft while maintaining the same swept area as the conventional Savonius model. This work by the author entitled "Numerical Investigation of Novel Design of Savonius Blade

Geometries for Vertical-Axis Wind Turbines" is accepted to ASME's PowerEnergy2016 conference.

4.3 Experimental RPM

Using the fixture shown in Figure 3.14 of the Methodology chapter, experimental RPM data is collected for all 6 VAWT models. The models are free to rotate with no applied load in this test. RPM vs. wind velocity data is presented in Figure 4.8.
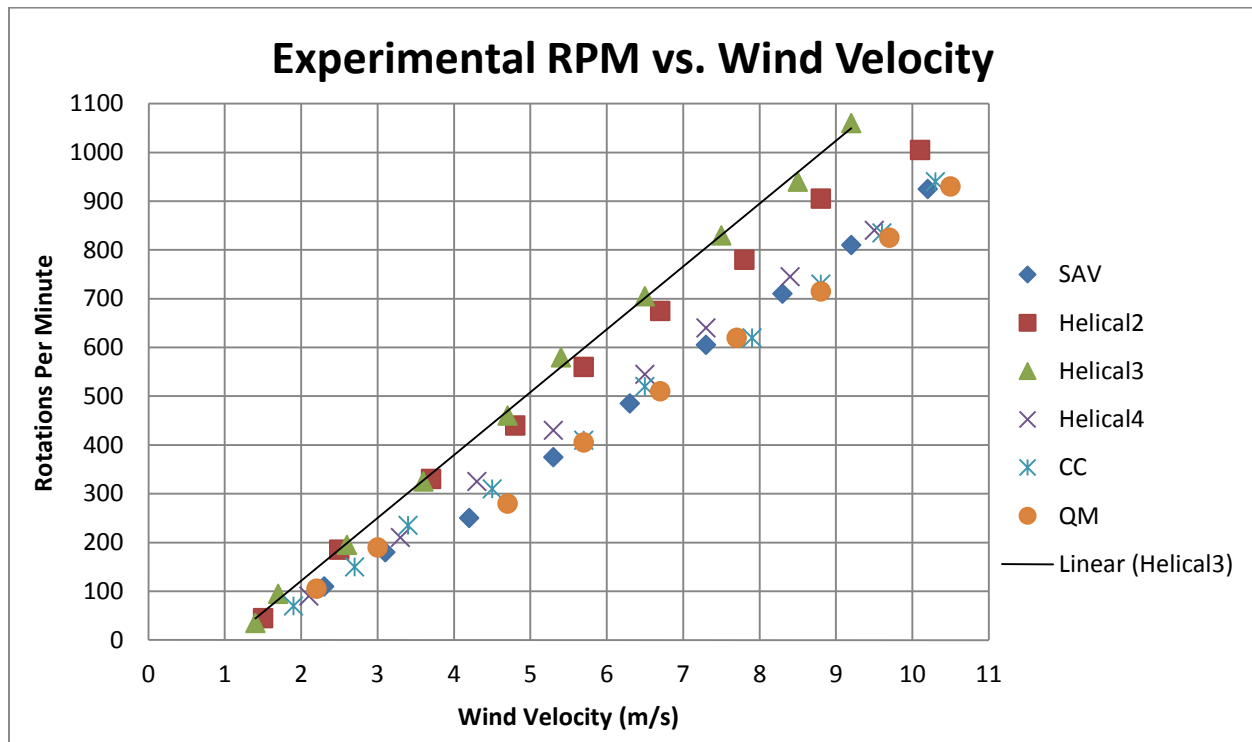
Figure 4.8. Experimental RPM vs. wind velocity for 6 models with no load

From the graph, it can be seen that the Helical3 and Helical2 models achieve the best self-starting characteristics in low wind speed conditions. Helical3 begins rotation at 1.4 m/s with 35 RPM, while Helical2 starts rotating at 1.5 m/s with 45 RPM. SAV has the worst self-starting capability in the study, beginning rotation at wind velocity of 2.3 m/s. At higher wind speeds, Helical3 achieves the fastest rotation of all 6 models. Helical2 and Helical3 both record significantly higher RPM than the other 4 models over the entire tested range of wind speeds.

4.4 Experimental torque

Each model is tested under varying wind conditions to determine the torque generated at every 10 degrees of model rotation. The reactional torque meter, shown in Figure 3.16 of Chapter 3, is used for the collection of experimental torque data. A schematic of model position relative to incoming wind velocity is displayed in Figure 4.9.
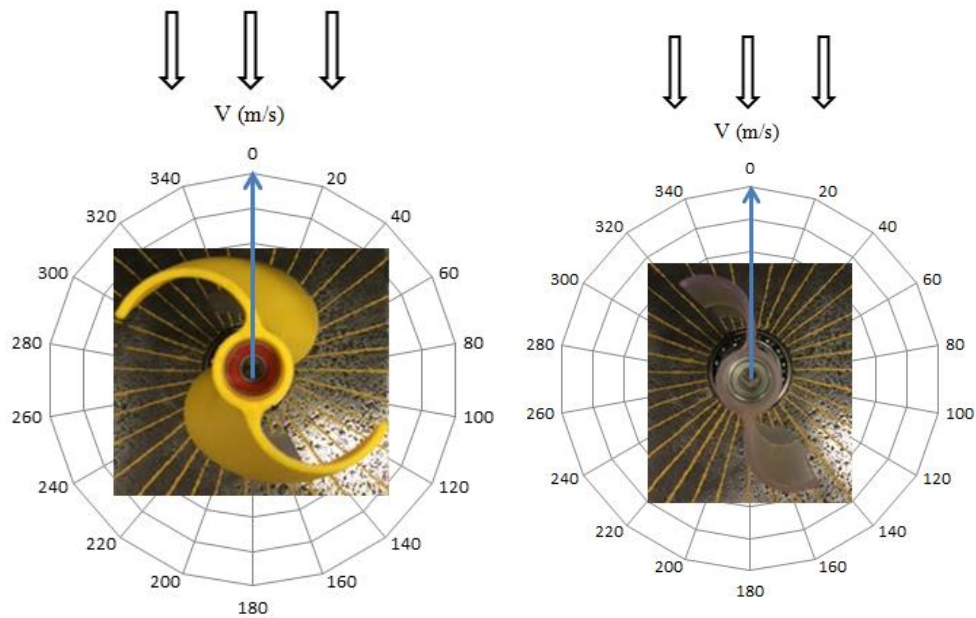
Figure 4.9. Schematic of VAWT blade angle relative to free stream velocity

The free-stream wind velocity is varied from 6 to 10 m/s. The torque data recorded for all 6 models are contained in Figures 4.10 - 4.15. The straight-bladed models, SAV, CC, and QM, all experience negative torque in 2 ranges of operation.
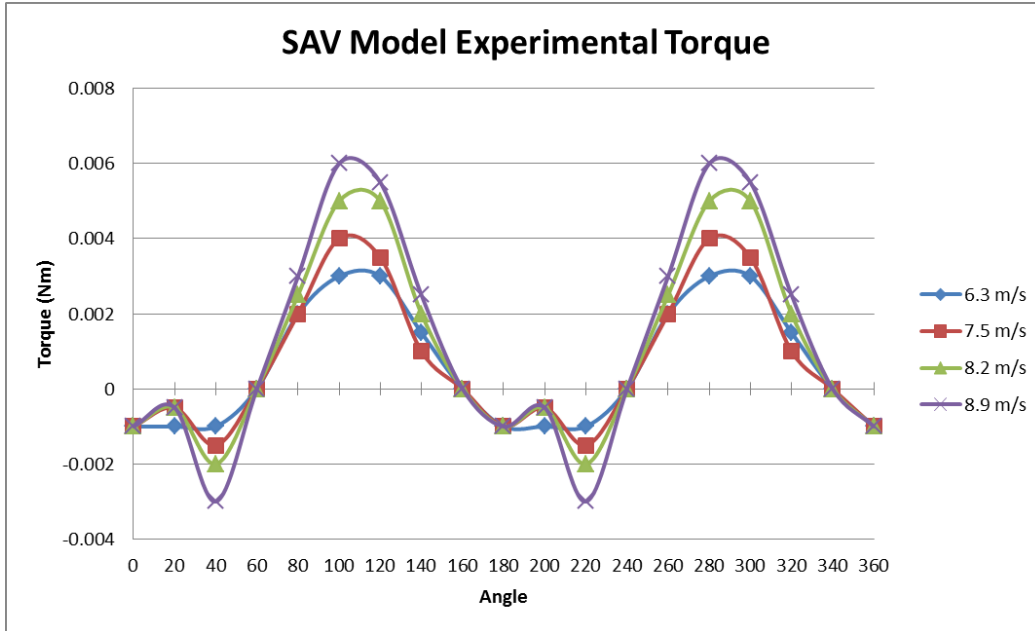
Figure 4.10. SAV model experimental torque data
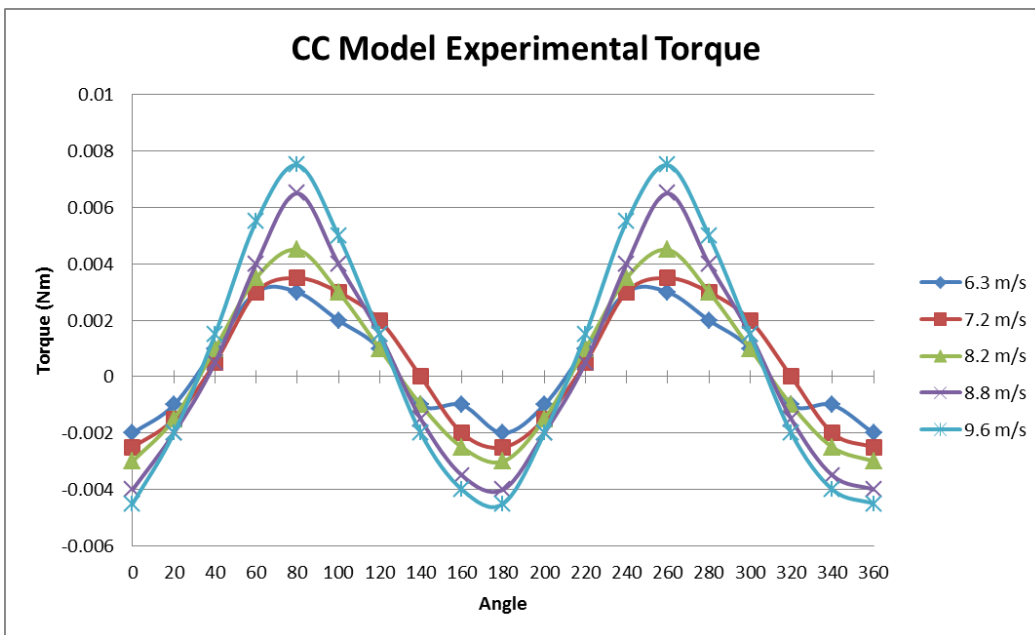
Figure 4.11. CC model experimental torque data
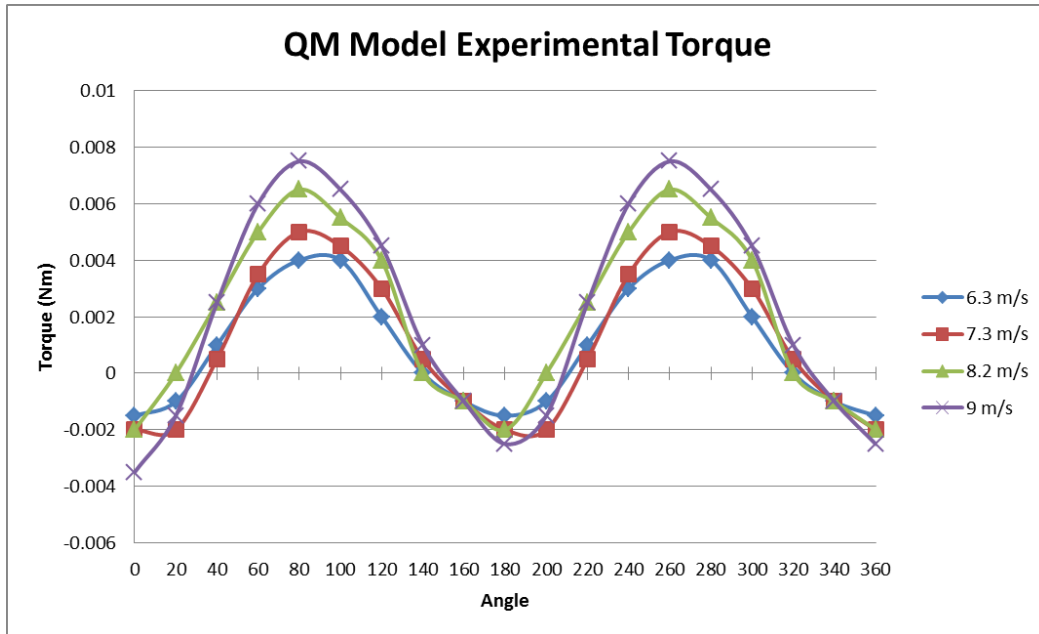
Figure 4.12. QM model experimental torque data
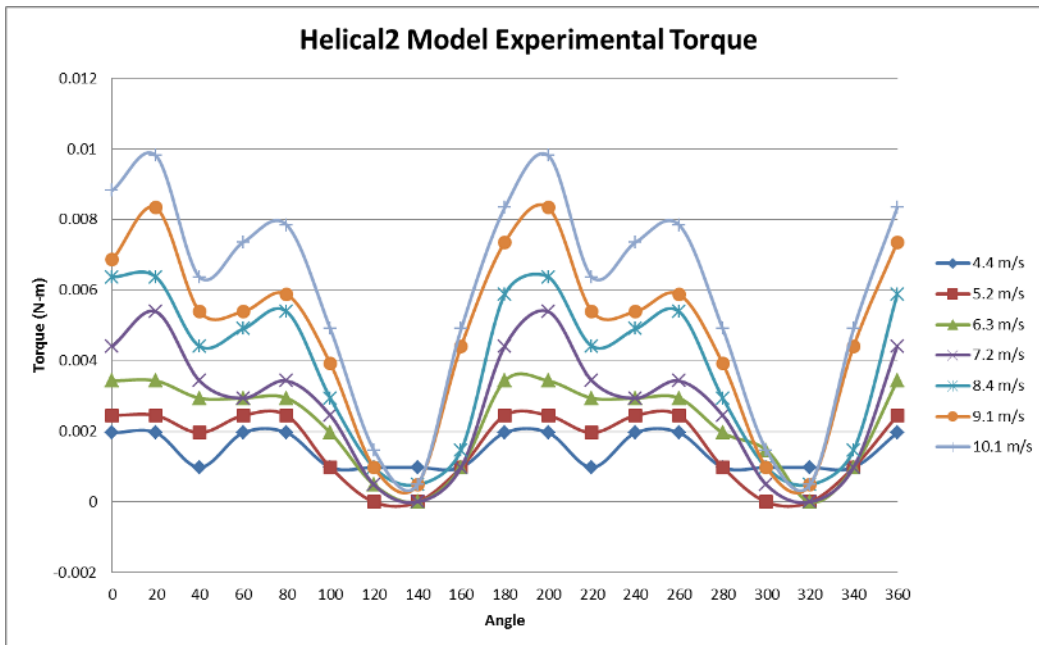
Figure 4.13. Helical2 model experimental torque data
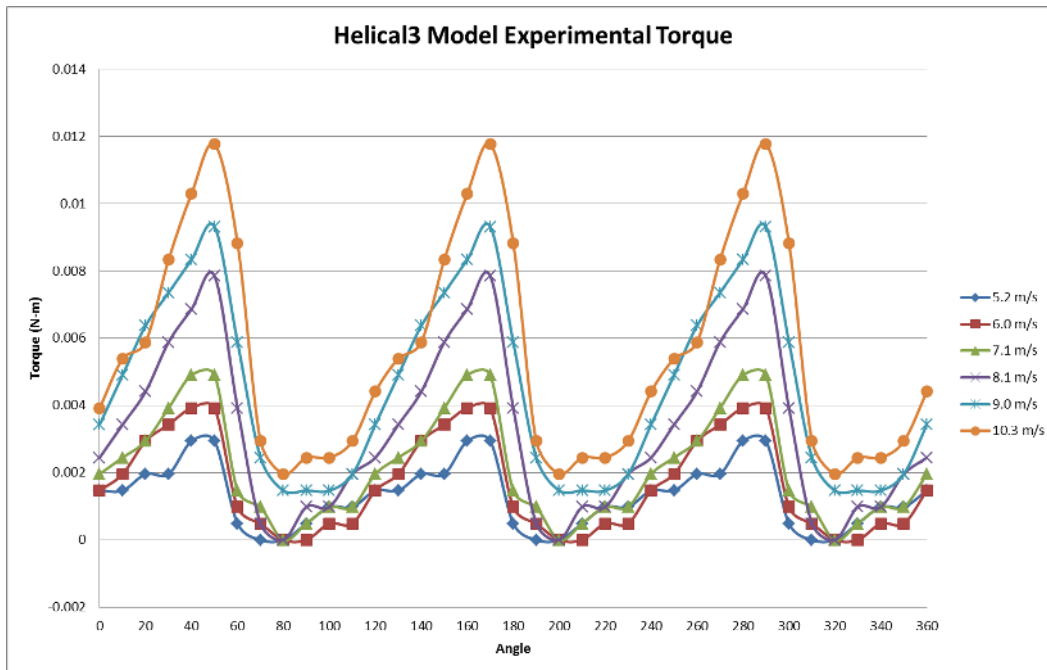
Figure 4.14. Helical3 model experimental torque data
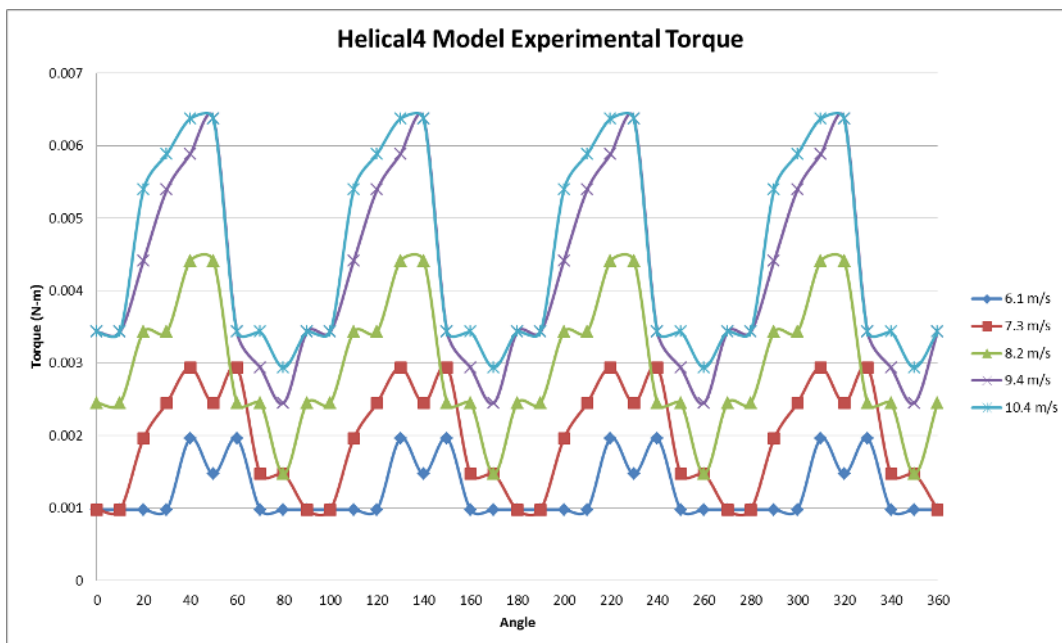
Figure 4.15. Helical4 model experimental torque data

As can be seen in Figures 4.13 – 4.15, all of the helical models experience positive torque for each angle of rotation. The Helical2 and Helical3 models generate significantly more torque than the Helical4 model at equivalent wind speeds.

4.5 Experimental coefficients of moment and power

The measured wind velocity, RPM, and torque data from the wind tunnel experiments are used to calculate the coefficient of moment and power for each turbine model. Moment coefficient is found from eq. 2, and power coefficient is found from eq. 5 in the methodology. Graphs of experimental moment coefficient vs. angle of rotation are displayed in Figures 4.16 – 4.21.
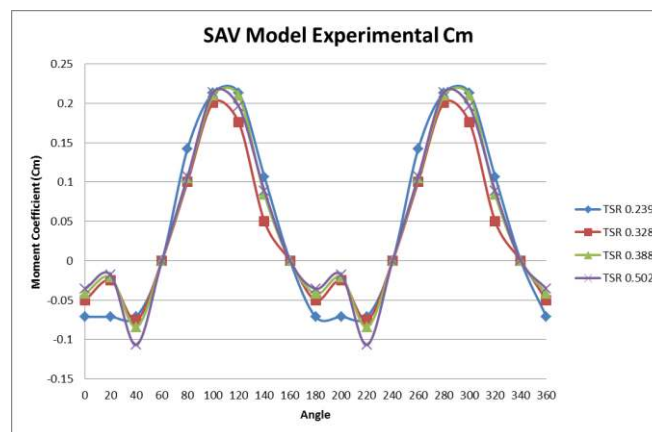
Figure 4.16. SAV model experimental moment coefficient
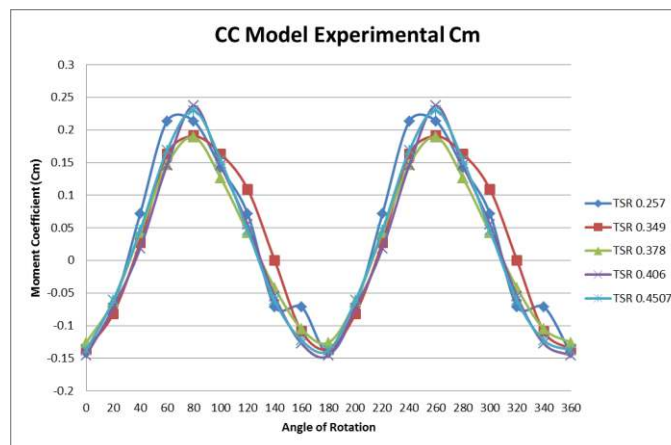
Figure 4.17. CC model experimental moment coefficient
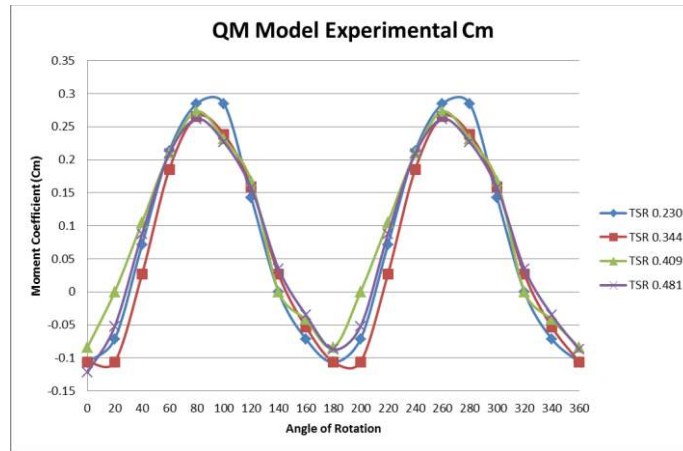
Figure 4.18. QM model experimental moment coefficient
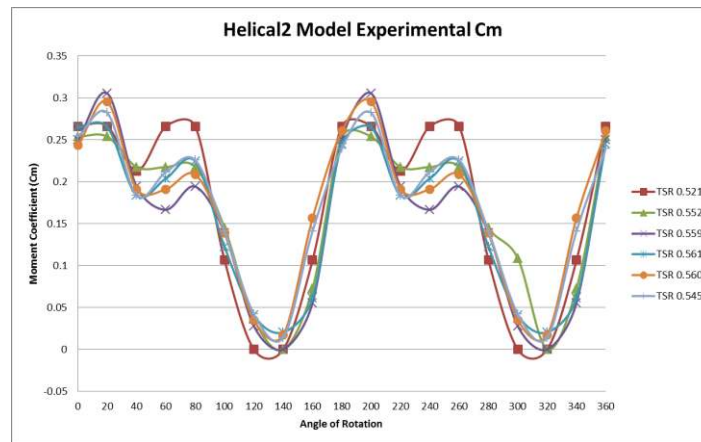
Figure 4.19. Helical2 experimental moment coefficient
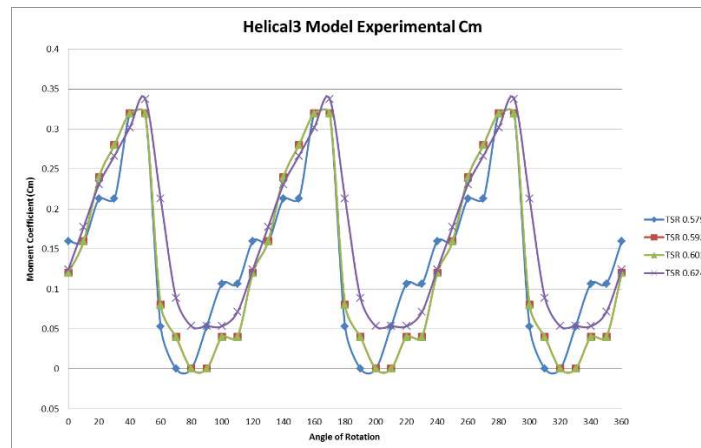
Figure 4.20. Helical3 experimental moment coefficient
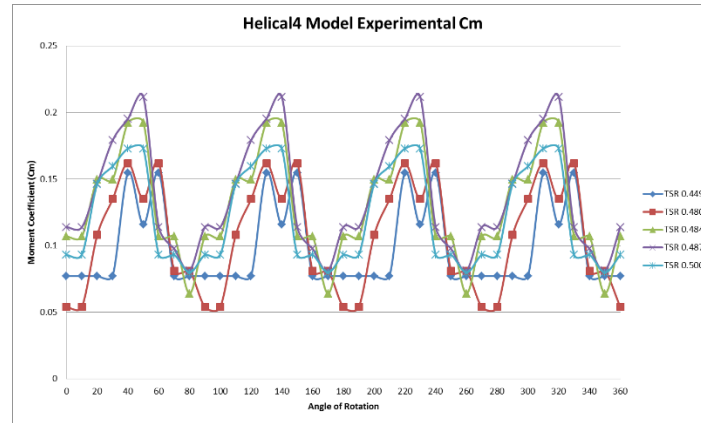
Figure 4.21. Helical4 experimental moment coefficient

In order to compare the experimental efficiencies of the models, experimental power coefficient

vs. tip-speed ratio for the 6 designs are plotted together in Figure 4.22.
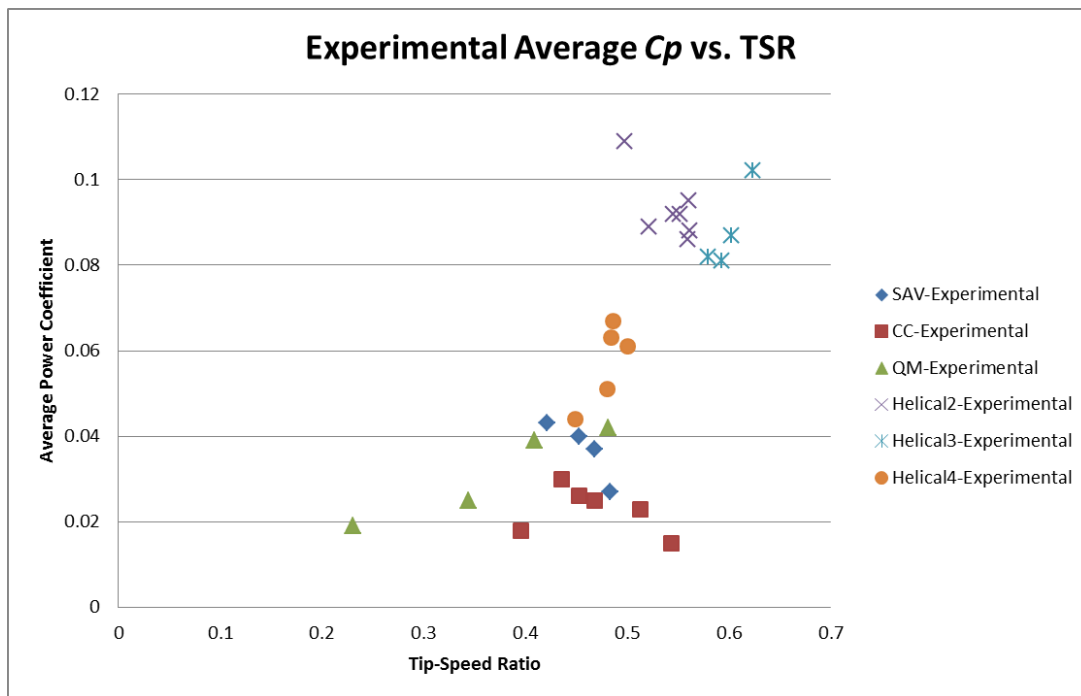
Figure 4.22. Experimental average power coefficient vs. tip-speed ratio for 6 model VAWTs

The Helical2 model achieves the highest experimental power coefficient of 0.109 at a tip-speed

ratio of 0.497. Maximum *Cp* for Helical3 is 0.102 at tip-speed ratio 0.623. The 90 degree helical

models with 2 and 3 blades perform significantly better than the other four models in the study.

4.6 Numerical study of helical blades

With experimental data for the helical models, numerical simulations with ANSYS Fluent are performed for validation of results. The same numerical methodology is used to obtain the following results; however, the wind velocity and corresponding RPM input boundary conditions are taken from the experimental data. This provides more realistic results for power coefficient vs. tip-speed ratio as the actual rotation of the VAWTs are modeled. Moment coefficient data from Fluent is used for calculating the average power coefficient for one full rotation. The results are plotted against corresponding tip-speed ratio in Figure 4.23.
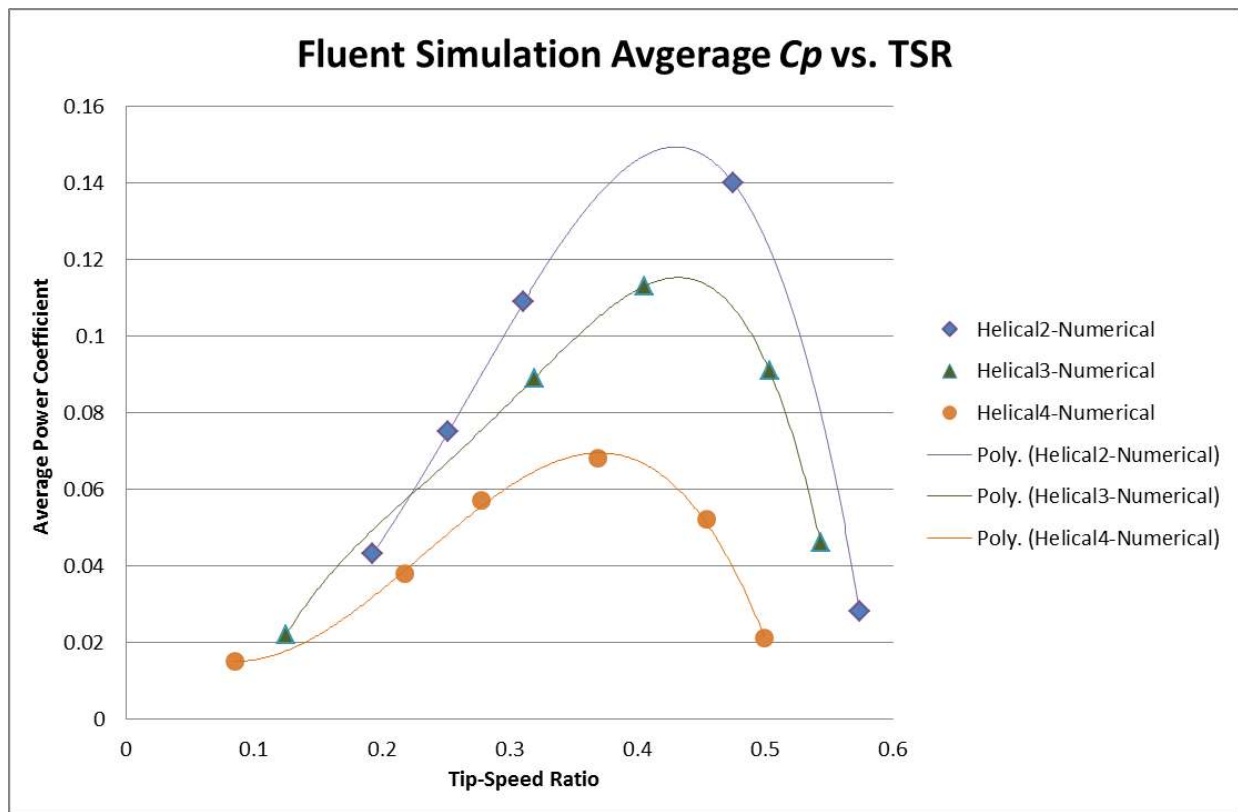
Figure 4.23. Fluent simulation power coefficient vs. tip-speed ratio for helical models

Each data set is fitted with a fourth order polynomial trend line to display the power curves for the numerical results of the helical models. The trend lines are defined by the following equations:

- Helical2: $y = -7.9302x^4 + 2.5854x^3 + 1.3819x^2 - 0.1032x + 0.0039$, $R^2 = 1$

- Helical3: $y = -24.641x^4 + 26.702x^3 - 10.558x^2 + 2.1185x - 0.124$, $R^2 = 1$

- Helical4: $y = -1.5723x^4 - 3.2814x^3 + 2.7944x^2 - 0.4011x + 0.0309$, $R^2 = 0.9972$

4.7 Pressure contours surrounding blades

This section contains the pressure contours surrounding the blades of the helical models. The cross-sections vary in the y-direction due to the blade twist, so three planes were created in post-processing for viewing results. The planes are located at the top, middle, and bottom of each model and are shown in Figure 4.24.
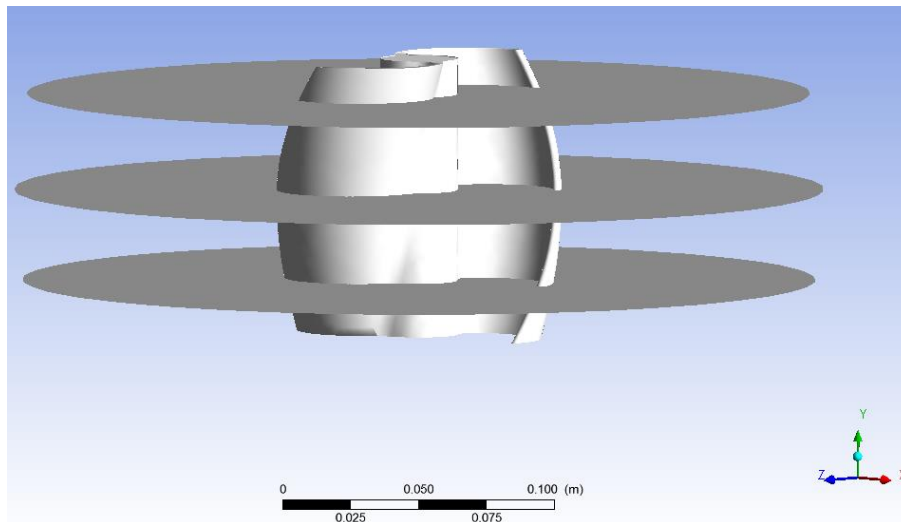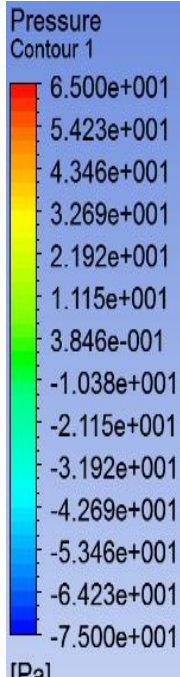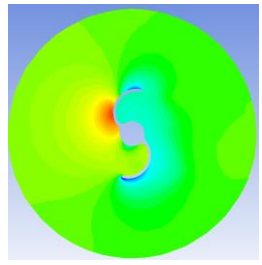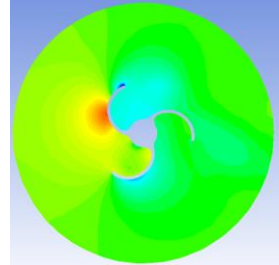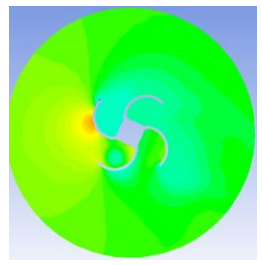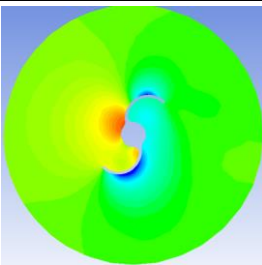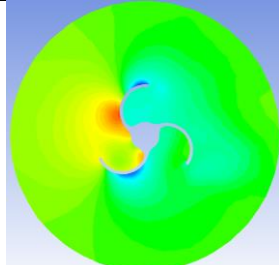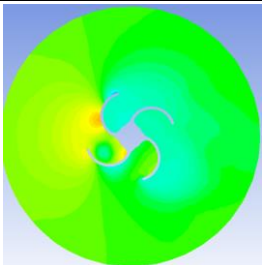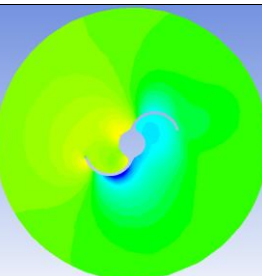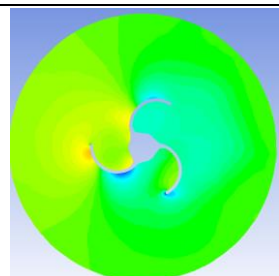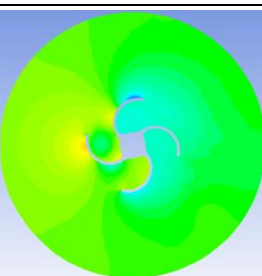
Figure 4.24. Planes a (top), b (middle), and c (bottom) for presenting helical model results

Pressure contours for the helical models at maximum power coefficient are presented in Table 4.5.

Table 4.5. Pressure contours for helical models at maximum power coefficients
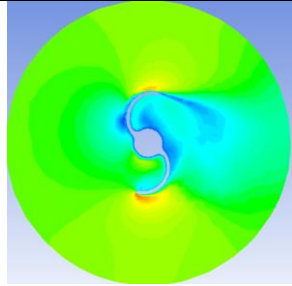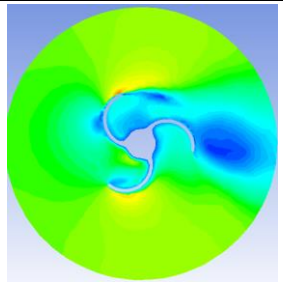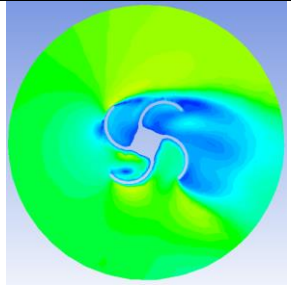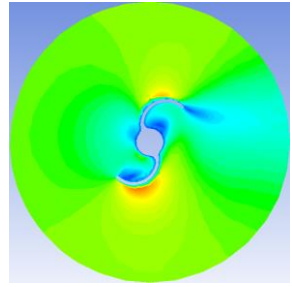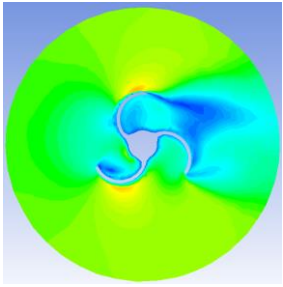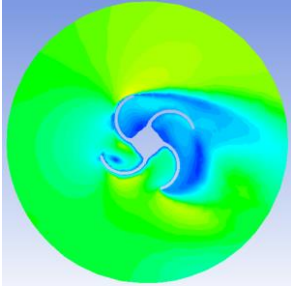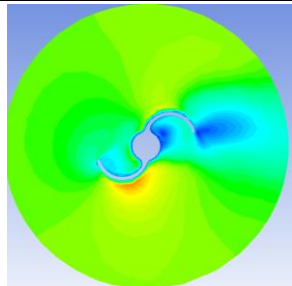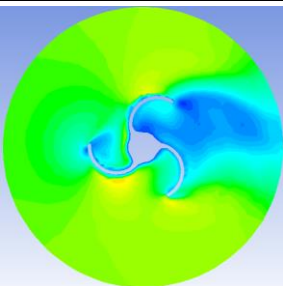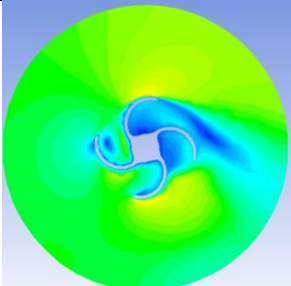
		Helical2	Helical3	Helical4
	Cp	0.140	0.113	0.068
	TSR	0.475	0.405	0.369
	Time	0.103s	0.135s	0.024s
Pressure Contour 1 6.500e+001 5.423e+001 4.346e+001 3.269e+001 2.192e+001 1.115e+001 3.846e-001 -1.038e+001 -2.115e+001 -3.192e+001 -4.269e+001 -5.346e+001 -6.423e+001 -7.500e+001 [Pa]	a			
	b			
	c			

The Helical2 model produces the highest power coefficient in the numerical study of 0.140. Seen in Table 4.5, a greater pressure is developed on the inside of the retreating blade, and more negative pressure is present on the backside. This results in larger pressure differential on the blade, compared to the other 2 models, allowing for the higher turbine efficiency.
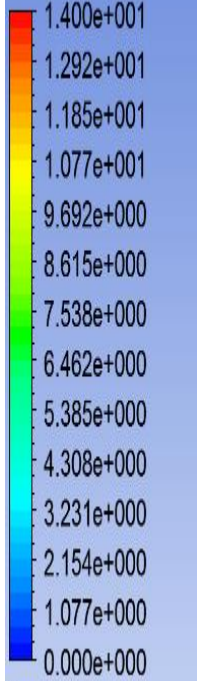
4.8 Air velocity surrounding blades

Air velocity contours and vectors are displayed in Tables 4.6 and 4.7, respectively.

Table 4.6. Velocity contours for helical models at maximum power coefficients

Model	Helical2	Helical3	Helical4
Cp	0.140	0.113	0.068
TSR	0.475	0.405	0.369
Time	0.103s	0.135s	0.024s
a			
b			
c			
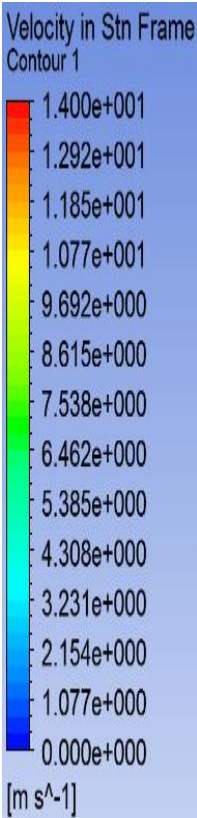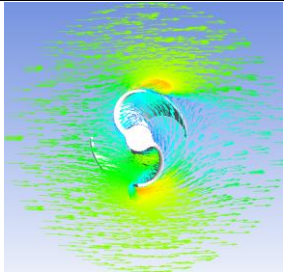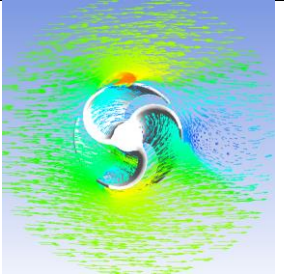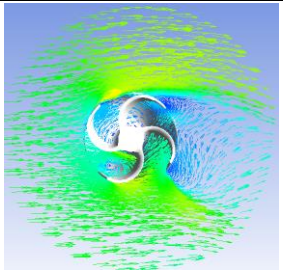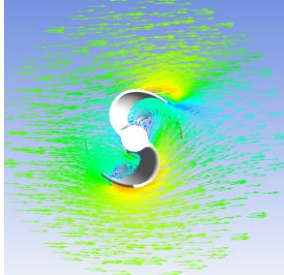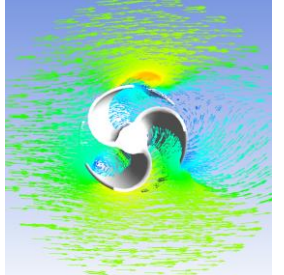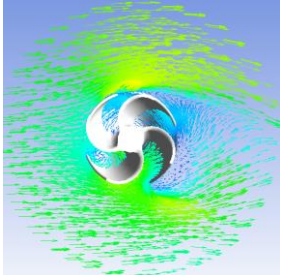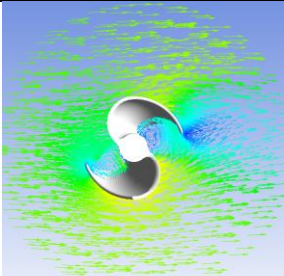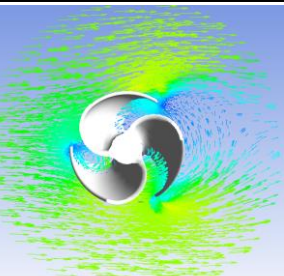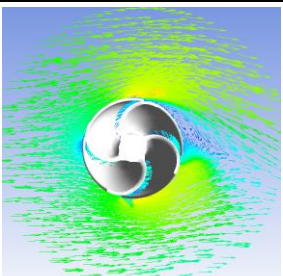
In all 3 planes, higher air velocity is present on the backside of the bottom blade for the Helical2 model. This creates the lower pressure seen in Table 4.5. The Helical3 and Helical4 models both produce significant wake behind the models, decreasing efficiency.

Table 4.7. Air velocity vectors for helical models at maximum power coefficients

		Helical2	Helical3	Helical4
	Cp	0.140	0.113	0.068
	TSR	0.475	0.405	0.369
	Time	0.103s	0.135s	0.024s
	a			
	b			
	c			

Velocity in Stn Frame
Contour 1

- 1.400e+001
- 1.292e+001
- 1.185e+001
- 1.077e+001
- 9.692e+000
- 8.615e+000
- 7.538e+000
- 6.462e+000
- 5.385e+000
- 4.308e+000
- 3.231e+000
- 2.154e+000
- 1.077e+000
- 0.000e+000
[m s^-1]

Vectors are shown along with contour plots to display air flow direction around the models. Air

swirling is present behind the helical models with 2 and 3 blades, reinforcing the observations stated before.

4.9 Comparison of experimental and numerical results for helical models

The experimental and numerical power coefficient results are plotted together with corresponding tip-speed ratios for the helical models in Figures 4.25 – 4.27.
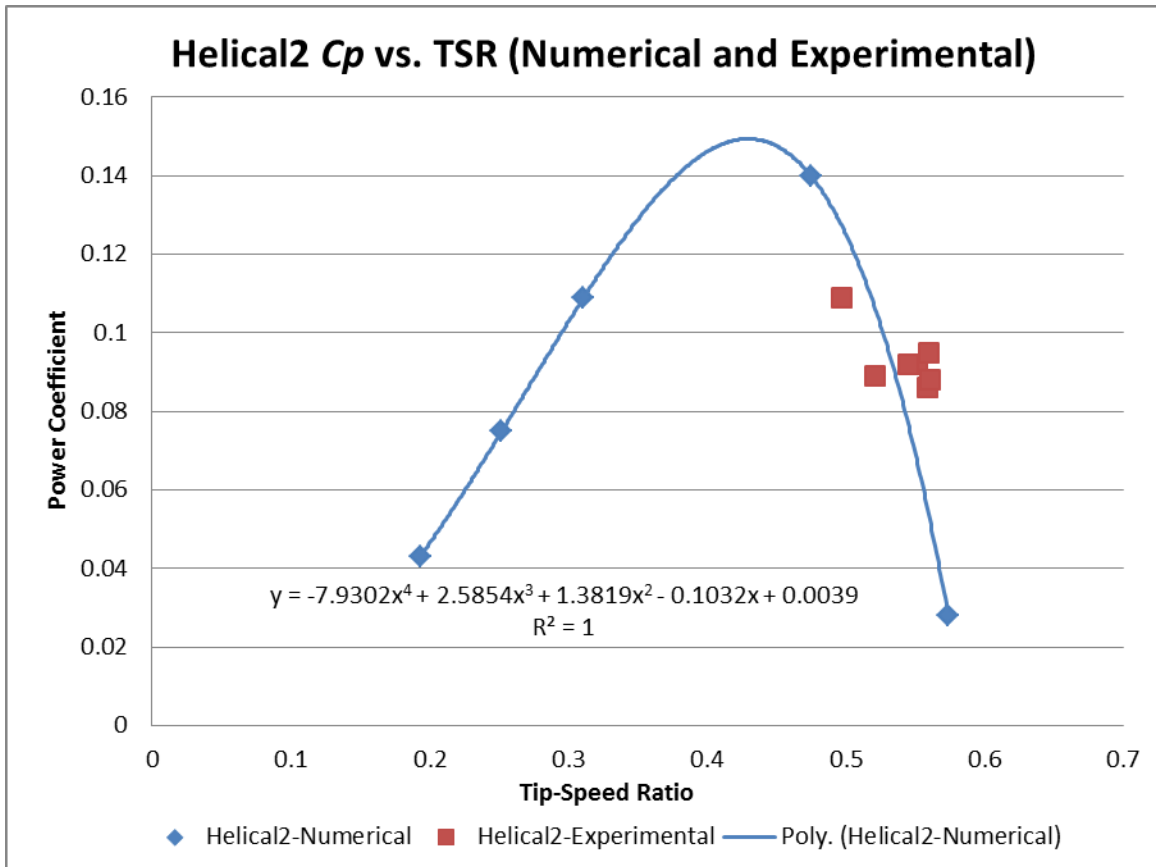
Figure 4.25. Numerical and experimental comparison for Helical2

For both numerical study and wind tunnel experimentation, the Helical2 model produces maximum power coefficient. Experimentally, maximum *Cp* of 0.109 is observed at TSR 0.497. Maximum *Cp* achieved for numerical simulation is 0.140 at TSR 0.475.
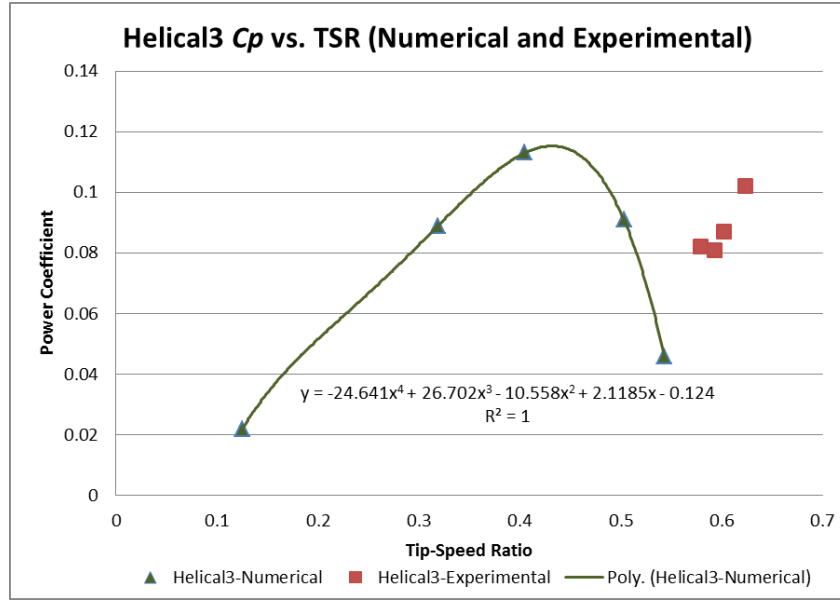
Figure 4.26. Numerical and experimental comparison for Helical3

Helical3 achieves maximum experimental *Cp* of 0.102 at TSR 0.623 and maximum numerical *Cp* of 0.113 at TSR 0.405.
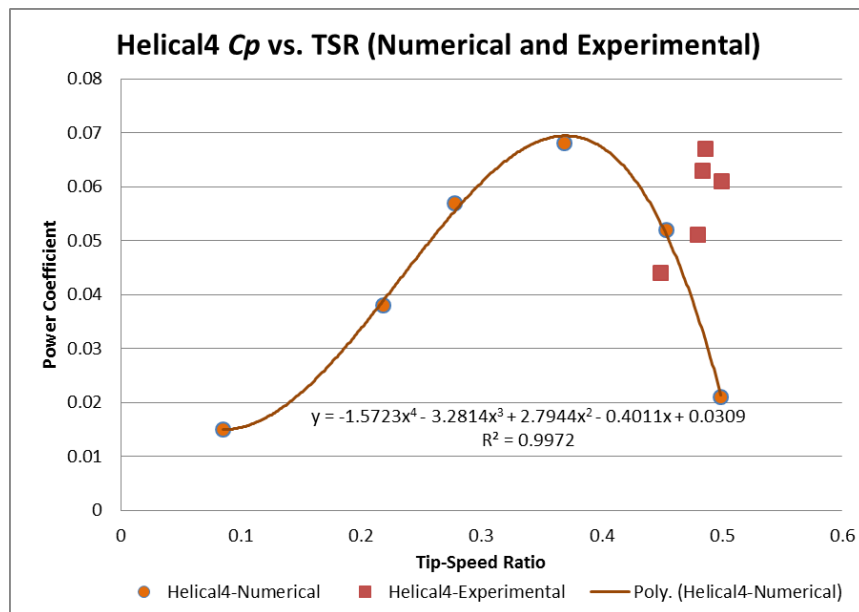
Figure 4.27. Numerical and experimental comparison for Helical4

Lowest efficiencies are observed with the Helical4 model: experimental *Cp* of 0.067 at TSR 0.486 and numerical *Cp* of 0.068 at TSR 0.369.

The Helical2 numerical results are plotted alongside the reported efficiency for traditional Savonius rotors from Figure 2.2 in the literature review. The comparison can be seen in Figure 4.28.
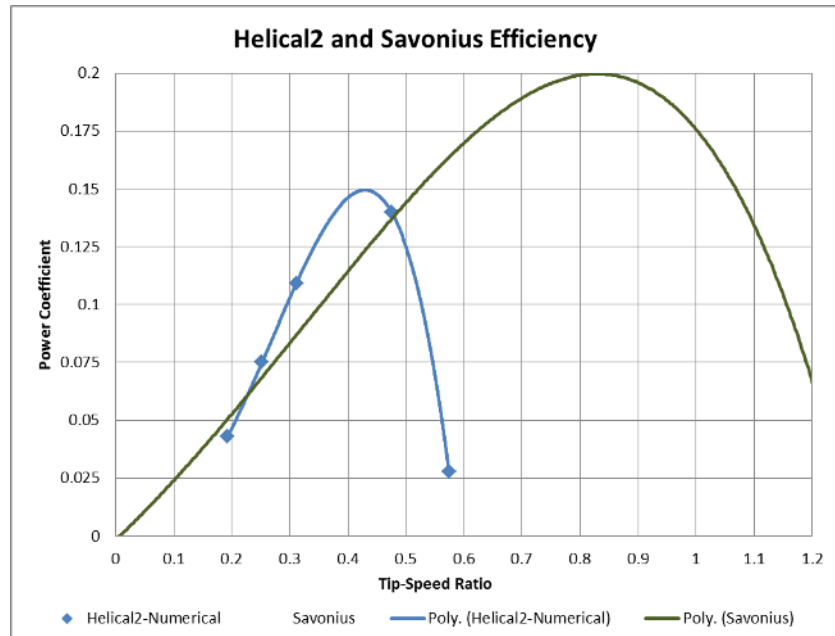
Figure 4.28 Helical2 and Savonius Efficiency

In terms of wind turbine efficiency, a performance increase is observed for the Helical2 model in the tip-speed ratio range of 0.25 to 0.475. At TSR 0.375, the helical turbine achieves just over a 3% increase in efficiency, compared to the traditional Savonius rotor.

CHAPTER 5

CONCLUSIONS AND RECOMMENDATIONS

5.1 Summary of work

This research investigates the performance of drag-based vertical-axis wind turbine (VAWT) models by experimental wind tunnel testing and conducting numerical simulations with ANSYS Fluent. Six different models are used in the study: three straight-blade Savonius style models with different blade geometries and three models of varying number of blades with 90 degree helical twist. The VAWT CAD models are designed with SolidWorks commercial software, and the physical models are 3D printed using FDM and SLA technologies. Methods for wind tunnel experiments and three-dimensional, transient numerical simulations are described in this work.

Initial ANSYS Fluent simulations are performed to validate concepts for the new CC and QM models. Self-starting capability of all 6 models is analyzed experimentally. Performance coefficients of the models are determined from wind tunnel testing. Experimental data is then used for input boundary conditions of the 3D numerical simulations.

5.2 Conclusions

The following conclusions are drawn from the study:

- The new QM and CC cross-section design for Savonius rotors create a center of pressure further from the axis of rotation, increasing power coefficient.

- Both the QM and CC designs reduce the total range of negative torque on the blades by 20 degrees, compared to the traditional SAV model.

- 90 degree helical twist models with 2-4 blades each experience positive torque for all angles of operation, while Savonius models experience negative torque in 2 regions.

- Helical2 and Helical3 possess the best self-starting capability.

    o Helical3: 35 RPM at 1.4 m/s wind velocity

    o Helical2: 45 RPM at 1.5 m/s wind velocity

- Highest average power coefficient observed in the study (1 complete rotation) is achieved by the Helical2 model, both numerically and experimentally.

    o Simulation: Cp = 0.140 at tip-speed ratio = 0.475

    o Wind tunnel experiment: Cp = 0.109 at tip-speed ratio = 0.497

- At TSR 0.375, the Helical2 turbine achieves just over a 3% increase in efficiency, compared to the reported efficiency of a traditional Savonius rotor. Increased power coefficient is observed for Helical2 in the tip-speed ratio range of 0.25 to 0.475.

5.3 Suggestions for future work

Based on the results of this thesis, it is recommended that new cross-sections such as the QM and CC designs be applied to helical twist blades. According to the literature review, performance may also be increased with the addition of circular end plates and a gap between the two blades. The aspect ratio, gap width, and twist angle should be varied to determine the optimal blade configuration. For experimental analysis, a dynamic torque sensor can be used to measure torque while the turbine is in operation, allowing for RPM to be recorded simultaneously. A new test fixture for the 3D printed models and dynamic torque sensor is currently under development for the GSU Wind Energy Laboratory. It is recommended that a braking system be applied to the load end of the torque sensor, allowing for better control of tip-speed ratios.

REFERENCES

Abraham, J. P., G. S. Mowry, B. P. Plourde, E. M. Sparrow, and W. J. Minkowycz. 2011. "Numerical simulation of fluid flow around a vertical-axis turbine." *Journal Of Renewable & Sustainable Energy* 3, no. 3: 033109. *Academic Search Complete*, EBSCO*host* (accessed November 3, 2014).

Alaimo, Andrea, Antonio Esposito, Antonio Messineo, Calogero Orlando, and Davide Tumino. 2015. "3D CFD Analysis of a Vertical Axis Wind Turbine." *Energies (19961073)* 8, no. 4: 3013-3033. *Academic Search Complete*, EBSCO*host* (accessed March 6, 2016).

Altan, Burçin Deda, and Mehmet Atılgan. 2008. "An experimental and numerical study on the improvement of the performance of Savonius wind rotor." *Energy Conversion & Management* 49, no. 12: 3425-3432. *Academic Search Complete*, EBSCO*host* (accessed November 9, 2014).

ANSYS Fluent Theory Guide—ANSYS Release Version 15.0, User's Guide; ANSYS Inc.: Canonsburg, PA, USA, 2012.

Armstrong, Shawn, Andrzej Fiedler, and Stephen Tullis. 2012. "Flow separation on a high Reynolds number, high solidity vertical axis wind turbine with straight and canted blades and canted blades with fences." *Renewable Energy: An International Journal* 41, 13-22. *Academic Search Complete*, EBSCO*host* (accessed November 9, 2014).

Bachu, Deb, Gupta Rajat, and Misra R. D. 2013. "PERFORMANCE ANALYSIS OF A HELICAL SAVONIUS ROTOR WITHOUT SHAFT AT 45° TWIST ANGLE USING CFD." *Journal Of Urban & Environmental Engineering* 7, no. 1: 126-133. *Environment Complete*, EBSCO*host* (accessed March 9, 2016).

Bashar, Mohammad M., Rahman, and Khan. 2013. "Computational Studies on the Flow Field of Various Shapes-Bladed Vertical Axis Savonius Turbine in Static Condition." *ASME 2013 International Mechanical Engineering Congress and Exposition*. San Diego, CA, USA, November 15-21, 2013.

Beri, Habtamu, and Yao Yingxue. 2011. "Numerical Simulation of Unsteady Flow to Show Self-starting of Vertical Axis Wind Turbine Using Fluent." *Journal Of Applied Sciences* 11, no. 6: 962-970. *Engineering Source*, EBSCO*host* (accessed November 9, 2014).

Bhuyan, S., and A. Biswas. 2014. "Investigations on self-starting and performance characteristics of simple H and hybrid H-Savonius vertical axis wind rotors." *Energy Conversion & Management* 87, 859-867. *Academic Search Complete*, EBSCO*host* (accessed November 3, 2014).

Can, Kang, Yang Xin, and Wang Yuli. 2013. "Turbulent Flow Characteristics and Dynamics Response of a Vertical-Axis Spiral Rotor." Energies (19961073) 6, no. 6: 2741-2758. Academic Search Complete, EBSCOhost (accessed March 8, 2016).

Deb, Bachu, Rajat Gupta, and R. D. Misra. 2014. "Experimental Analysis of a 20° Twist Helical Savonius Rotor at Different Overlap Conditions." *Applied Mechanics & Materials*no. 592-594: 1060-1064. *Engineering Source*, EBSCO*host* (accessed March 6, 2016).

Díaz, Palencia, Argemiro, Giovanni Jiménez Pajaro, and Khriscia Utria Salas. 2015. "Computational model of Savonius turbine." *INGENIARE - Revista Chilena De Ingeniería*23, no. 3: 406-412. *Academic Search Complete*, EBSCO*host* (accessed March 6, 2016).

FLUENT Manual—ANSYS Release Version 15.0, User's Guide; ANSYS Inc.: Canonsburg, PA, USA, 2012.

Gavaldà, Jna., J. Massons, and F. Díaz. 1990. "Experimental study on a self-adapting Darrieus—Savonius wind machine." *Solar And Wind Technology* 7, 457-461. *ScienceDirect*, EBSCO*host* (accessed November 9, 2014).

Ghatage, Swapnil V., and Jyeshtharaj B. Joshi. 2012. "Optimisation of vertical axis wind turbine: CFD simulations and experimental measurements." *Canadian Journal Of Chemical Engineering* 90, no. 5: 1186-1201. *Engineering Source*, EBSCO*host* (accessed November 9, 2014).

Gorelov, D., and V. Krivospitsky. 2008. "Prospects for development of wind turbines with orthogonal rotor." *Thermophysics & Aeromechanics* 15, no. 1: 153. *Publisher Provided Full Text Searching File*, EBSCO*host* (accessed November 5, 2014).

Gupta, R., A. Biswas, and K.K. Sharma. 2008. "Comparative study of a three-bucket Savonius rotor with a combined three-bucket Savonius–three-bladed Darrieus rotor." *Renewable Energy: An International Journal* 33, no. 9: 1974-1981. *Academic Search Complete*, EBSCO*host* (accessed November 5, 2014).

Islam, Mazharul, David S.-K. Ting, and Amir Fartaj. 2008. "Aerodynamic models for Darrieus-type straight-bladed vertical axis wind turbines." *Renewable & Sustainable Energy Reviews* 12, no. 4: 1087-1109. *Academic Search Complete*, EBSCO*host* (accessed November 9, 2014).

Jeon, Keum Soo, Jun Ik Jeong, Jae-Kyung Pan, and Ki-Wahn Ryu. 2014. "Effects of end plates with various shapes and sizes on helical Savonius wind turbines." *Renewable Energy*ScienceDirect*, EBSCO*host* (accessed March 6, 2016).

Kamoji, M.A., S.B. Kedare, and S.V. Prabhu. 2009. "Performance tests on helical Savonius rotors." *Renewable Energy* 34, 521-529. *ScienceDirect*, EBSCO*host* (accessed March 10, 2016).

Kou, Wei, Xinchun Shi, Bin Yuan, and Lintao Fan. 2011. "Modeling analysis and experimental research on a combined-type vertical axis wind turbine." *2011 International Conference On Electronics, Communications & Control (ICECC)* 1537. *Publisher Provided Full Text Searching File*, EBSCO*host* (accessed November 3, 2014).

Lee, Jae-Hoon, Young-Tae Lee, and Hee-Chang Lim. 2016. "Effect of twist angle on the performance of Savonius wind turbine." *Renewable Energy* 89, 231-244. *ScienceDirect*, EBSCO*host* (accessed March 8, 2016).

MacPhee, David, and Asfaw Beyene. 2012. "Recent Advances in Rotor Design of Vertical Axis Wind Turbines." *Wind Engineering* 36, no. 6: 647-666. *Environment Complete*, EBSCO*host* (accessed November 3, 2014).

Mohamed, M.H. 2012. "Performance investigation of H-rotor Darrieus turbine with new airfoil shapes." *Energy* 47, no. 1: 522-530. *Academic Search Complete*, EBSCO*host* (accessed November 9, 2014).

Morshed, K. N., M. Rahman, G. M. and M. Ahmed, Wind Tunnel Testing and Numerical Simulation on Aerodynamic Performance of a Three Bladed Savonius Wind Turbine," International Journal of Energy and Environmental Engineering, 2013, pp. 4-18.

Pope, K., G. F. Naterer, I. Dincer, and E. Tsang. 2011. "Power correlation for vertical axis wind turbines with varying geometries." *International Journal Of Energy Research* 35, no. 5: 423-435. *Environment Complete*, EBSCO*host* (accessed November 9, 2014).

Ricci, Renato, Roberto Romagnoli, Sergio Montelpare, and Daniele Vitali. 2016. "Experimental study on a Savonius wind rotor for street lighting systems." *Applied Energy* 161, 143-152. *Environment Complete*, EBSCO*host* (accessed March 10, 2016).

Rui-Tao, Deng, Song Lei, Yang Zong-Xiao, Yang Hang-Hang, and Wang Long-Biao. 2011. "Research and development of a simple straight-flow wind tunnel test equipment for vertical axis wind turbines." *International Conference On Advanced Mechatronic Systems (Icamechs), 2011* 250. *Publisher Provided Full Text Searching File*, EBSCO*host* (accessed November 7, 2014).

Sagol E, Reggio M, Ilinca A. "Assessment of Two-Equation Turbulence Models and Validation of the Performance Characteristics of an Experimental Wind Turbine by CFD." *ISRN Mechanical Engineering* [serial online]. January 2012; 1.

Saha, U.K., and M. Jaya Rajkumar. 2006. "On the performance analysis of Savonius rotor with twisted blades." *Renewable Energy* 31, 1776-1788.*ScienceDirect*, EBSCO*host* (accessed March 9, 2016).

Saha, U., Thotla, S., & Maity, D. (2008). "Optimum design configuration of Savonius rotor through wind tunnel experiments." *Journal Of Wind Engineering & Industrial Aerodynamics*, *96*1359-1375. doi:10.1016/j.jweia.2008.03.005

Wenehenubun, Frederikus, Andy Saputra, and Hadi Sutanto. 2015. "An Experimental Study on the Performance of Savonius Wind Turbines Related With The Number Of Blades." Energy Procedia 68, no. 2nd International Conference on Sustainable Energy Engineering and Application (ICSEEA) 2014 Sustainable Energy for Green Mobility: 297-304. ScienceDirect, EBSCOhost (accessed March 9, 2016).

"Wind Vision: A New Era for Wind Power in the United States." ENERGY.GOV. Accessed April 7, 2016. http://energy.gov/eere/wind/maps/wind-vision.

APPENDICES

Appendix A: List of Publications

The following is a list of publications related to the work described in this thesis:

1. Rahman, M., **Salyers, T.,** Maroha, E., and Ahmed, M., "Investigation of Aerodynamic Performance of Helical Shape Vertical-Axis Wind Turbine Models with Various Number of Blades Using Wind Tunnel Testing and Computational Fluid Dynamics," submitted for publication in the ***proceedings of the ASME 2016 International Mechanical Engineering Congress and Exposition (IMECE 2016)***, Phoenix, AZ, USA, November 11-17, 2016.

2. Rahman, M., **Salyers, T.,** Maroha, E., Ahmed, M., and Salekeen, S., "Numerical Investigation of Novel Blade Geometry Design of Vertical Axis Wind Turbines for Performance Improvement," accepted for publication in the ***proceedings of the ASME 2016 Power and Energy Conference (PowerEnergy2016),*** Charlotte, NC, USA, June 26-30, 2016.

3. Rahman, M., **Salyers, T.,** and Maroha, E., "Experimental Set-Up Design and Testing of Vertical and Horizontal Axis Wind Turbine Models in a Subsonic Wind Tunnel," ***proceedings of the 2016 ASEE Southeast Section Conference, "Engineering for Sustainability,"*** The University of Alabama, Tuscaloosa, AL, USA, March 13-15, 2016.

4. Rahman, M., Basher, M., Molina, G., Soloiu, V., and **Salyers, T.,** "Numerical Investigation on Vertical Axis Wind Turbine in Search for an Efficient Design," ***proceedings of the ASME 2015 International Mechanical Engineering Congress and Exposition (IMECE 2015),*** *Houston, Texas, USA, November 13-19, 2015.*

Appendix B: Improvements to the GSU Wind Tunnel

The first improvement to GSU's wind energy laboratory was the addition of a new test section for the existing wind tunnel. The entire frame was built by students in the machine shop on campus. The first step was cutting purchased material, shown in Figure 1B, to design specifications with a horizontal band saw.

Figure 1B. Material for new wind tunnel section construction

Steel tubing for the base of the frame is being cut in the band saw in Figure 2B. Also, a CNC plasma cutter was used for cutting four steel plates with bolt holes to which casters were fastened at the bottom of the structure.

Figure 2B. Cutting material with horizontal band saw

Angle steel was then welded to create the outside flanges which connect the frame with the existing wind tunnel. The inlet and outlet of the testing section measure 40" x 40". Square steel tubing was used to add strength to the base as well as the bottom of the tunnel. A 12" x 12" steel plate was welded in place in the center of the testing section to provide support for various fixtures for all types of experiments. Construction of the frame and the completed test section on casters are shown in Figures 3B and 4B.

Figure 3B. Construction of angle steel frame

Figure 4B. Completed test section frame on casters

After completion of the project build, the frame was moved to the renewable energy research lab.

Displayed in Figure 5B, the new tunnel section was connected with the existing wind tunnel. The

new positioning of models inside the wind tunnel and directly behind a honeycomb section

provides more consistent, laminar airflow for experiments.

Figure 5B. New test section installed with existing wind tunnel

The steel plate, centered in the test section, for supporting several new fixtures is pictured in

Figure 6B.
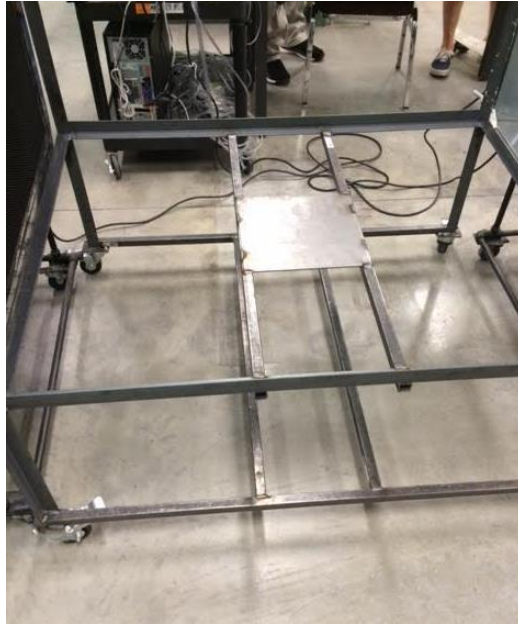
Figure 6B. Supports and steel plate in center of test section

The section was then painted and acrylic doors were bolted on the frame, shown in Figure 7B.

Figure 7B. Addition of clear acrylic doors (left) and painted frame (right)

The completed test section is displayed in Figure 8B.

Figure 8B. Front (left) and back (right) photos of completed model testing section

Several new fixtures were fabricated for use in the wind energy lab. Researchers needed a new fixture to support dynamic torque experiments. The old set-up, displayed in Figure 9B, experienced too much vibration in the system and friction in the bearings. It also consisted of a long, 0.5 in. diameter steel shaft which did not allow smaller 3D printed models to rotate.

Figure 9B. Existing dynamic torque set-up with shaft, coupling, torque sensor, and generator

A new fixture for dynamic torque measurement was designed with SolidWorks. The CAD model of the entire torque measurement assembly can be seen in Figure 10B.
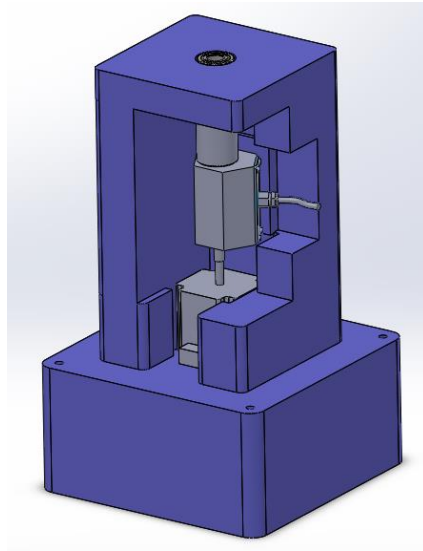
Figure 10B. CAD model of new dynamic torque measurement fixture

The CAD files for the fixture were sent out to be 3D printed. During that process, an additional fixture was made out of wood to contain a smaller generator for testing of the 3D printed models. The wooden fixture is displayed in Figure 11B.
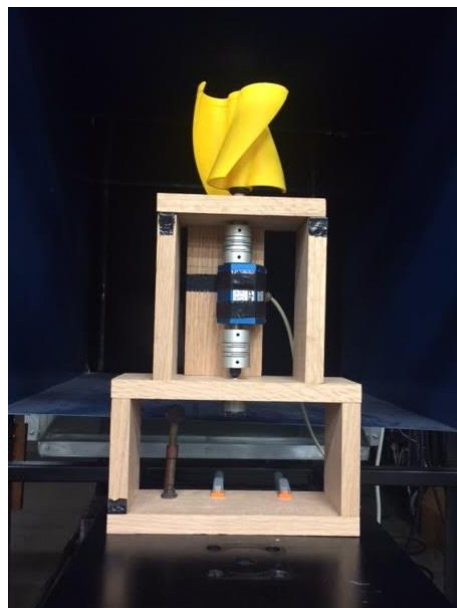
Figure 11B. Wooden fixture for dynamic torque measurement of smaller 3D printed VAWTs

New experimental set-ups were developed for RPM measurement as well. A laser tachometer is shown in Figure 12B recording rotations per minute with a VAWT producing power from a small DC motor.
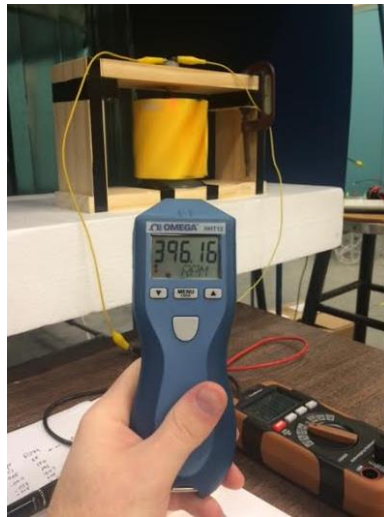
Figure 12B. RPM measurement fixture with load

An additional stand was acquired to measure RPM of 3D models under no load condition to evaluate self-starting capabilities.
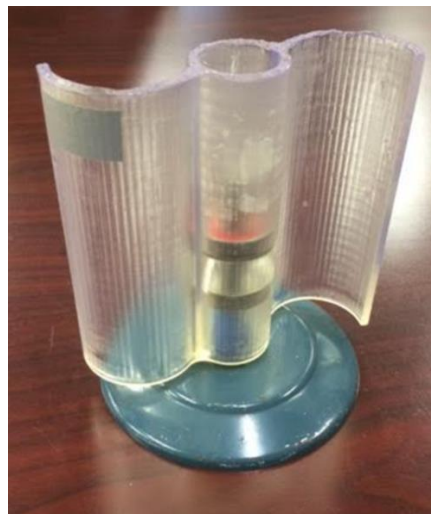
Figure 13B. RPM measurement of models under no load

Appendix C: VAWT Simulation Data for Initial Numerical Study with Constant RPM

Table 1E. SAV Model Data for 275 RPM and 3, 5, and 7 m/s

SAV Model					
3m/s		5m/s		7m/s	
Time (s)	*Cm*	Time (s)	*Cm*	Time (s)	*Cm*
0.003	-0.11137	0.003	-0.18049	0.003	-0.17139
0.006	-0.10828	0.006	-0.18440	0.006	-0.18853
0.009	-0.10453	0.009	-0.18686	0.009	-0.20195
0.012	-0.09989	0.012	-0.18753	0.012	-0.21171
0.015	-0.09422	0.015	-0.18544	0.015	-0.21560
0.018	-0.08722	0.018	-0.17928	0.018	-0.21032
0.021	-0.07859	0.021	-0.16762	0.021	-0.19327
0.024	-0.06767	0.024	-0.14999	0.024	-0.16673
0.027	-0.05417	0.027	-0.12759	0.027	-0.12772
0.030	-0.03868	0.030	-0.09953	0.030	-0.08414
0.033	-0.02119	0.033	-0.06868	0.033	-0.03690
0.036	-0.00274	0.036	-0.03596	0.036	0.01254
0.039	0.01630	0.039	-0.00142	0.039	0.06208
0.042	0.03479	0.042	0.03370	0.042	0.10917
0.045	0.05234	0.045	0.06776	0.045	0.14936
0.048	0.06837	0.048	0.09855	0.048	0.18259
0.051	0.08221	0.051	0.12557	0.051	0.20793
0.054	0.09353	0.054	0.14815	0.054	0.23418
0.057	0.10134	0.057	0.16987	0.057	0.28062
0.060	0.10571	0.060	0.19678	0.060	0.36408
0.063	0.10787	0.063	0.23321	0.063	0.48778
0.066	0.10936	0.066	0.28068	0.066	0.63972
0.069	0.11142	0.069	0.33719	0.069	0.80360
0.072	0.11455	0.072	0.39873	0.072	0.96444
0.075	0.11907	0.075	0.45844	0.075	1.10401
0.078	0.12481	0.078	0.50976	0.078	1.20214
0.081	0.13022	0.081	0.54521	0.081	1.24825
0.084	0.13355	0.084	0.55964	0.084	1.23149
0.087	0.13370	0.087	0.55057	0.087	1.15176
0.090	0.12832	0.090	0.51435	0.090	1.01259
0.093	0.11839	0.093	0.45293	0.093	0.82666
0.096	0.10251	0.096	0.36971	0.096	0.60903
0.099	0.08111	0.099	0.26862	0.099	0.38007
0.102	0.05548	0.102	0.15548	0.102	0.16117
0.105	0.02742	0.105	0.04338	0.105	-0.03001

0.108	-0.00273	0.108	-0.05573	0.108	-0.19320
0.111	-0.03275	0.111	-0.13249	0.111	-0.29946
0.114	-0.05978	0.114	-0.18329	0.114	-0.34872
0.117	-0.08159	0.117	-0.20285	0.117	-0.35616
0.120	-0.09547	0.120	-0.19606	0.120	-0.34011
0.123	-0.09959	0.123	-0.17814	0.123	-0.31062
0.126	-0.09572	0.126	-0.15574	0.126	-0.27370
0.129	-0.08566	0.129	-0.13043	0.129	-0.22431
0.132	-0.07148	0.132	-0.09895	0.132	-0.16503
0.135	-0.05419	0.135	-0.06246	0.135	-0.10043
0.138	-0.03531	0.138	-0.02182	0.138	-0.03305
0.141	-0.01600	0.141	0.02109	0.141	0.03187
0.144	0.00293	0.144	0.06330	0.144	0.09066
0.147	0.02084	0.147	0.10233	0.147	0.14461
0.150	0.03702	0.150	0.13628	0.150	0.19387
0.153	0.05094	0.153	0.16428	0.153	0.23940
0.156	0.06257	0.156	0.18756	0.156	0.28115
0.159	0.07128	0.159	0.20569	0.159	0.32054
0.162	0.07722	0.162	0.21991	0.162	0.36087
0.165	0.08087	0.165	0.23303	0.165	0.41003
0.168	0.08298	0.168	0.25030	0.168	0.48101
0.171	0.08432	0.171	0.27570	0.171	0.58383
0.174	0.08550	0.174	0.31220	0.174	0.71265
0.177	0.08783	0.177	0.35842	0.177	0.85221
0.180	0.09141	0.180	0.40905	0.180	0.99098
0.183	0.09606	0.183	0.45896	0.183	1.10735
0.186	0.10120	0.186	0.50089	0.186	1.18405
0.189	0.10558	0.189	0.53005	0.189	1.21417
0.192	0.10811	0.192	0.53933	0.192	1.18920
0.195	0.10729	0.195	0.52637	0.195	1.10877
0.198	0.10108	0.198	0.48991	0.198	0.98147
0.201	0.08869	0.201	0.42918	0.201	0.81550
0.204	0.07041	0.204	0.34829	0.204	0.62047
0.207	0.04722	0.207	0.25193	0.207	0.40774
0.210	0.02069	0.210	0.14536	0.210	0.19921
0.213	-0.00774	0.213	0.03519	0.213	0.00758
0.216	-0.03658	0.216	-0.06508	0.216	-0.16105
0.219	-0.06347	0.219	-0.14270	0.219	-0.28660

Table 2E. CC Model Data for 275 RPM and 3, 5, and 7 m/s

CC Model					
3m/s		5m/s		7m/s	
Time (s)	*Cm*	Time (s)	*Cm*	Time (s)	*Cm*
0.003	-0.11710	0.003	-0.09865	0.003	-0.09257
0.006	-0.11666	0.006	-0.10597	0.006	-0.11540
0.009	-0.11572	0.009	-0.11212	0.009	-0.13422
0.012	-0.11360	0.012	-0.11679	0.012	-0.14657
0.015	-0.11018	0.015	-0.11874	0.015	-0.15052
0.018	-0.10481	0.018	-0.11677	0.018	-0.14311
0.021	-0.09707	0.021	-0.10905	0.021	-0.12228
0.024	-0.08640	0.024	-0.09409	0.024	-0.08561
0.027	-0.07242	0.027	-0.07074	0.027	-0.03344
0.030	-0.05491	0.030	-0.03864	0.030	0.03292
0.033	-0.03428	0.033	0.00124	0.033	0.11172
0.036	-0.01069	0.036	0.04825	0.036	0.19843
0.039	0.01491	0.039	0.10042	0.039	0.28966
0.042	0.04129	0.042	0.15685	0.042	0.37901
0.045	0.06741	0.045	0.21184	0.045	0.45887
0.048	0.09215	0.048	0.26257	0.048	0.52269
0.051	0.11429	0.051	0.30471	0.051	0.56849
0.054	0.13269	0.054	0.33630	0.054	0.59920
0.057	0.14638	0.057	0.35736	0.057	0.62137
0.060	0.15442	0.060	0.37045	0.060	0.64563
0.063	0.15675	0.063	0.37969	0.063	0.68294
0.066	0.15441	0.066	0.38992	0.066	0.74437
0.069	0.14938	0.069	0.40476	0.069	0.83053
0.072	0.14348	0.072	0.42535	0.072	0.94398
0.075	0.13827	0.075	0.45109	0.075	1.05844
0.078	0.13465	0.078	0.48181	0.078	1.16031
0.081	0.13298	0.081	0.51163	0.081	1.22720
0.084	0.13309	0.084	0.53119	0.084	1.23805
0.087	0.13260	0.087	0.53483	0.087	1.18435
0.090	0.12939	0.090	0.51662	0.090	1.06394
0.093	0.12182	0.093	0.47000	0.093	0.89207
0.096	0.10889	0.096	0.39384	0.096	0.69780
0.099	0.09077	0.099	0.29789	0.099	0.51133
0.102	0.06795	0.102	0.19780	0.102	0.35258
0.105	0.04135	0.105	0.10987	0.105	0.21592
0.108	0.01310	0.108	0.03733	0.108	0.07659
0.111	-0.01504	0.111	-0.02544	0.111	-0.05538

0.114	-0.04086	0.114	-0.08177	0.114	-0.17446
0.117	-0.06271	0.117	-0.12932	0.117	-0.27463
0.120	-0.07866	0.120	-0.16651	0.120	-0.34599
0.123	-0.08772	0.123	-0.18949	0.123	-0.38165
0.126	-0.08978	0.126	-0.19674	0.126	-0.38024
0.129	-0.08572	0.129	-0.18701	0.129	-0.34552
0.132	-0.07636	0.132	-0.16258	0.132	-0.28252
0.135	-0.06256	0.135	-0.12711	0.135	-0.20164
0.138	-0.04498	0.138	-0.08179	0.138	-0.10805
0.141	-0.02423	0.141	-0.03048	0.141	-0.00884
0.144	-0.00131	0.144	0.02424	0.144	0.09122
0.147	0.02269	0.147	0.08130	0.147	0.19007
0.150	0.04686	0.150	0.13845	0.150	0.28690
0.153	0.06955	0.153	0.19391	0.153	0.38035
0.156	0.08988	0.156	0.24551	0.156	0.46582
0.159	0.10659	0.159	0.29040	0.159	0.53875
0.162	0.11885	0.162	0.32593	0.162	0.59461
0.165	0.12631	0.165	0.35133	0.165	0.63681
0.168	0.12914	0.168	0.36805	0.168	0.67252
0.171	0.12840	0.171	0.38036	0.171	0.71226
0.174	0.12557	0.174	0.39329	0.174	0.76957
0.177	0.12193	0.177	0.41119	0.177	0.85722
0.180	0.11841	0.180	0.43684	0.180	0.97925
0.183	0.11563	0.183	0.46883	0.183	1.11589
0.186	0.11411	0.186	0.50658	0.186	1.24555
0.189	0.11369	0.189	0.54569	0.189	1.34550
0.192	0.11311	0.192	0.57851	0.192	1.39032
0.195	0.11066	0.195	0.59385	0.195	1.36072
0.198	0.10460	0.198	0.58469	0.198	1.25368
0.201	0.09366	0.201	0.54455	0.201	1.08212
0.204	0.07726	0.204	0.47104	0.204	0.87208
0.207	0.05588	0.207	0.37203	0.207	0.65874
0.210	0.03072	0.210	0.26590	0.210	0.47220
0.213	0.00337	0.213	0.16969	0.213	0.31983
0.216	-0.02413	0.216	0.09143	0.216	0.18341
0.219	-0.04928	0.219	0.02653	0.219	0.04398

Table 3E. QM Model Data for 275 RPM and 3, 5, and 7 m/s

QM Model					
3m/s		5m/s		7m/s	
Time (s)	*Cm*	Time (s)	*Cm*	Time (s)	*Cm*
0.003	-0.12560	0.003	-0.11185	0.003	-0.10716
0.006	-0.12572	0.006	-0.11975	0.006	-0.12745
0.009	-0.12546	0.009	-0.12625	0.009	-0.14490
0.012	-0.12454	0.012	-0.13088	0.012	-0.15842
0.015	-0.12220	0.015	-0.13198	0.015	-0.16485
0.018	-0.11776	0.018	-0.12803	0.018	-0.15977
0.021	-0.11102	0.021	-0.11817	0.021	-0.14273
0.024	-0.10109	0.024	-0.10093	0.024	-0.10974
0.027	-0.08762	0.027	-0.07581	0.027	-0.05835
0.030	-0.07060	0.030	-0.04295	0.030	0.00755
0.033	-0.04989	0.033	-0.00292	0.033	0.08510
0.036	-0.02625	0.036	0.04292	0.036	0.17170
0.039	-0.00037	0.039	0.09376	0.039	0.26421
0.042	0.02666	0.042	0.14762	0.042	0.35761
0.045	0.05381	0.045	0.20171	0.045	0.44258
0.048	0.07968	0.048	0.25147	0.048	0.51122
0.051	0.10286	0.051	0.29232	0.051	0.56092
0.054	0.12231	0.054	0.32264	0.054	0.59477
0.057	0.13701	0.057	0.34296	0.057	0.61951
0.060	0.14639	0.060	0.35718	0.060	0.64678
0.063	0.14982	0.063	0.37132	0.063	0.68913
0.066	0.14872	0.066	0.39163	0.066	0.75766
0.069	0.14493	0.069	0.42248	0.069	0.85800
0.072	0.13995	0.072	0.46454	0.072	0.97952
0.075	0.13568	0.075	0.51376	0.075	1.11081
0.078	0.13286	0.078	0.56374	0.078	1.23046
0.081	0.13234	0.081	0.60539	0.081	1.30913
0.084	0.13352	0.084	0.62754	0.084	1.32640
0.087	0.13442	0.087	0.62186	0.087	1.27112
0.090	0.13241	0.090	0.58370	0.090	1.14360
0.093	0.12556	0.093	0.51463	0.093	0.95728
0.096	0.11297	0.096	0.41996	0.096	0.74695
0.099	0.09426	0.099	0.31250	0.099	0.55271
0.102	0.07041	0.102	0.20873	0.102	0.39096
0.105	0.04284	0.105	0.12098	0.105	0.24443
0.108	0.01360	0.108	0.04962	0.108	0.09621
0.111	-0.01529	0.111	-0.01437	0.111	-0.03977

0.114	-0.04186	0.114	-0.07117	0.114	-0.16311
0.117	-0.06395	0.117	-0.11998	0.117	-0.26842
0.120	-0.08071	0.120	-0.16031	0.120	-0.34419
0.123	-0.09111	0.123	-0.18622	0.123	-0.38305
0.126	-0.09495	0.126	-0.19500	0.126	-0.38523
0.129	-0.09228	0.129	-0.18582	0.129	-0.35248
0.132	-0.08391	0.132	-0.16145	0.132	-0.29433
0.135	-0.07063	0.135	-0.12588	0.135	-0.21566
0.138	-0.05333	0.138	-0.08231	0.138	-0.12465
0.141	-0.03269	0.141	-0.03308	0.141	-0.02779
0.144	-0.00985	0.144	0.01979	0.144	0.07012
0.147	0.01414	0.147	0.07528	0.147	0.16751
0.150	0.03860	0.150	0.13164	0.150	0.26342
0.153	0.06210	0.153	0.18708	0.153	0.35663
0.156	0.08352	0.156	0.23885	0.156	0.44465
0.159	0.10160	0.159	0.28309	0.159	0.52191
0.162	0.11529	0.162	0.31652	0.162	0.58204
0.165	0.12392	0.165	0.33873	0.165	0.62575
0.168	0.12791	0.168	0.35360	0.168	0.66264
0.171	0.12842	0.171	0.36825	0.171	0.70809
0.174	0.12664	0.174	0.38954	0.174	0.77595
0.177	0.12395	0.177	0.42283	0.177	0.87810
0.180	0.12124	0.180	0.46911	0.180	1.01615
0.183	0.11933	0.183	0.52398	0.183	1.17359
0.186	0.11868	0.186	0.58047	0.186	1.32034
0.189	0.11913	0.189	0.62947	0.189	1.43077
0.192	0.11996	0.192	0.66060	0.192	1.47409
0.195	0.11873	0.195	0.66413	0.195	1.43794
0.198	0.11331	0.198	0.63426	0.198	1.32170
0.201	0.10257	0.201	0.56935	0.201	1.13360
0.204	0.08582	0.204	0.47457	0.204	0.90171
0.207	0.06359	0.207	0.36251	0.207	0.67581
0.210	0.03694	0.210	0.25150	0.210	0.48835
0.213	0.00811	0.213	0.15728	0.213	0.34188
0.216	-0.02075	0.216	0.08213	0.216	0.19821
0.219	-0.04706	0.219	0.01745	0.219	0.05662